Biomaterials 287 (2022) 121674

Contents lists available at ScienceDirect

Biomaterials

journal homepage: www.elsevier.com/locate/biomaterials

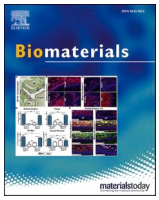

Macromolecular crowding transforms regenerative medicine by enabling the accelerated development of functional and truly three-dimensional cell assembled micro tissues

Andrea De Pieri [a,b,c], Stefanie H. Korntner [a,b], Hector Capella-Monsonis [a,b], Dimitrios Tsiapalis [a,b], Sergei V. Kostjuk [d,e], Semyon Churbanov [e], Peter Timashev [e], Alexander Gorelov [f], Yuri Rochev [b,e], Dimitrios I. Zeugolis [a,b,g,*]

[a] *Regenerative, Modular & Developmental Engineering Laboratory (REMODEL), Biomedical Sciences Building, National University of Ireland Galway (NUI Galway), Galway, Ireland*
[b] *Science Foundation Ireland (SFI) Centre for Research in Medical Devices (CÚRAM), Biomedical Sciences Building, National University of Ireland Galway (NUI Galway), Galway, Ireland*
[c] *Proxy Biomedical Ltd., Spiddal, Galway, Ireland*
[d] *Department of Chemistry, Belarusian State University and Research Institute for Physical Chemical Problems of the Belarusian State University, Minsk, Belarus*
[e] *Institute for Regenerative Medicine, Sechenov First Moscow State Medical University (Sechenov University), Moscow, Russia*
[f] *School of Chemistry & Chemical Biology, University College Dublin, Dublin, Ireland*
[g] *Regenerative, Modular & Developmental Engineering Laboratory (REMODEL), Charles Institute of Dermatology, Conway Institute of Biomolecular & Biomedical Research and School of Mechanical & Materials Engineering, University College Dublin (UCD), Dublin, Ireland*

ARTICLE INFO

Keywords:
Temperature-responsive polymers
Electrospinning
Macromolecular crowding
Excluded volume effect
In vitro organogenesis

ABSTRACT

Scaffold-free *in vitro* organogenesis exploits the innate ability of cells to synthesise and deposit their own extracellular matrix to fabricate tissue-like assemblies. Unfortunately, cell-assembled tissue engineered concepts require prolonged *ex vivo* culture periods of very high cell numbers for the development of a borderline three-dimensional implantable device, which are associated with phenotypic drift and high manufacturing costs, thus, hindering their clinical translation and commercialisation. Herein, we report the accelerated (10 days) development of a truly three-dimensional (338.1 ± 42.9 μm) scaffold-free tissue equivalent that promotes fast wound healing and induces formation of neotissue composed of mature collagen fibres, using human adipose derived stem cells seeded at only 50,000 cells/cm^2 on an poly (*N*-isopropylacrylamide-co-*N*-*tert*-butylacrylamide (PNIPAM86-NTBA14) temperature-responsive electrospun scaffold and grown under macromolecular crowding conditions (50 μg/ml carrageenan). Our data pave the path for a new era in scaffold-free regenerative medicine.

1. Introduction

Cell-based therapies, either as cell-alone injections or as cell-scaffold combinations, are at the forefront of scientific research and technological innovation in regenerative medicine to treat, augment or replace a lost, due to disease or injury, tissue function [1–5]. Despite the numerous positive preclinical and clinical results in a diverse range of clinical indications, the mode of administration of injected cell suspensions offers poor control over cell protection and localisation at the site of implantation and the use of artificial scaffolds triggers adverse immune responses [6–8]. To overcome these limitations, the concept of scaffold-free *in vitro* organogenesis has been pioneered that allows for the production of tissue-like assemblies *in vitro*, by exploiting the inherent ability of cells to synthesise and deposit their own extracellular matrix (ECM) [9–11].

Traditionally, the production of three-dimensional (3D) scaffold-free tissue equivalents for non-load-bearing tissues is a two-step process. Firstly, single cell sheets are produced using surfaces coated with temperature-responsive polymers, which upon reduction of the temperature below the lower critical solution temperature (LCST) of the polymer allow for the detachment of intact cells and deposited ECM thin layers [12–15]. Then, by layering multiple cell sheets together and

* Corresponding author. Regenerative, Modular & Developmental Engineering Laboratory (REMODEL), Biomedical Sciences Building, National University of Ireland Galway (NUI Galway), Galway, Ireland.
E-mail address: dimitrios.zevgolis@ucd.ie (D.I. Zeugolis).

https://doi.org/10.1016/j.biomaterials.2022.121674
Received 29 November 2021; Received in revised form 3 July 2022; Accepted 6 July 2022
Available online 9 July 2022
0142-9612/© 2022 The Authors. Published by Elsevier Ltd. This is an open access article under the CC BY license (http://creativecommons.org/licenses/by/4.0/).

culturing them for the required maturation time, 3D tissue-like assemblies are realised [16,17]. Despite the positive outcomes, with respect to safety and therapeutic efficacy, of scaffold-free *in vitro* organogenesis approaches in preclinical and clinical setting, only a handful of products have been commercialised [18]. This limited technology transfer from laboratories to clinics has been attributed to numerous factors. For example, it is still technically challenging to produce multi-layered cell sheets in reproducible fashion. The creation of thick enough multi-layered cell sheets not only requires millions of cells, frequently not available for autologous applications, but also is associated with limited nutrient, waste and oxygen transfer in the middle layers, which results in cell death [19] and delamination [20]. Consequently, multiple operations of up to 3 layers are recommended [21], which again require high cell numbers, are barely at the 3D range and are associated with prolonged patient distress and high healthcare expenditure. It is therefore eminent and timely to develop technologies that will allow for full exploitation of the *in vitro* organogenesis concept.

Electrospinning produces 3D fibrous constructs that closely imitate native tissues architectural features and the high porosity of the resultant scaffolds allows for appropriate nutrient, waste and oxygen transport [22–24]. Although electrospinning of temperature-responsive polymers has enabled the development of scaffold-free cell layers [25,26], a commercially and clinically viable tissue-like surrogate is still onerous. This may be attributed to the large numbers of cells still required and the prolonged time in culture needed for the cells to deposit sufficient ECM that is associated with cell phenotype losses [27,28]. Considering that ECM is key modulator of cell fate [29–32], strategies that integrate enhanced and accelerated ECM synthesis and deposition in the developmental cycle of *in vitro* organogenesis concepts may be able to bridge the gap between positive therapeutic clinical efficacy and market success.

Although various *in vitro* microenvironment modulators have been assessed over the years as a means to control cell fate in culture, only marginally (e.g. growth factor supplementation [33], oxygen tension [34–37], mechanical stimulation [38]), if at all (e.g. surface topography, substrate rigidity), enhance and accelerate ECM synthesis and deposition. To this end, the concept of macromolecular crowding (MMC) has been introduced that, following the principles of excluded volume effect, accelerates biochemical reactions and biological processes by several orders of magnitude [39–45]. Although MMC, by imitating the localised density of native tissues *in vitro*, has been shown to induce an up to 120-fold increase in collagen and associated ECM deposition within 4–6 days in differentiated [46–50] and stem [34,51–57] cell cultures, its safety and efficacy in regenerative medicine has yet to be assessed.

Herein, we report the development of a truly 3D tissue substitute, using only a fraction of cells and time that customary *in vitro* organogenesis approaches utilise, by culturing human adipose derived stem cells (hADSCs) onto a temperature-responsive electrospun scaffold under MMC conditions. The therapeutic efficacy and safety of the produced tissue-like supramolecular assemblies were validated in a mouse excisional wound splinting model.

2. Materials and methods

2.1. Materials

All chemicals, cell culture media and reagents were purchased from Sigma Aldrich (Ireland), and used as received, unless otherwise stated. Tissue culture consumables were purchased from Sarstedt (Ireland) and NUNC (Denmark).

2.2. Synthesis and characterisation of temperature-responsive copolymers

Poly (*N*-isopropylacrylamide-*co*-*N*-*tert*-butylacrylamide (PNIPAM-NTBA) copolymers were synthesised and characterised as has been described before [36,37]. *N*-isopropylacrylamide was recrystallized from *n*-hexane, *N*-*tert*-butylacrylamide (Acros, 97%) was recrystallized from acetone under argon atmosphere and 2,2′-azobisisobutyronitrile (Merck, >98%) was recrystallized from ethanol. The copolymers were prepared by free radical polymerisation using azobisisobutyronitrile as an initiator in benzene. After polymerisation at 60 °C for 24 h, the mixture was precipitated in *n*-hexane. The obtained copolymers were then purified by dissolving in acetone followed by precipitation in *n*-hexane for at least 3 times and the product was dried at 45 °C in a vacuum oven. Two copolymers were synthesised in this work containing 14 mol % (PNIPAM86-NTBA14) and 32 mol % (PNIPAM68-NTBA32) of *N*-*tert*-butylacrylamide, respectively. The composition of copolymers was confirmed by ^{1}H NMR spectroscopy. The number-average molecular weight and polydispersity were determined by size exclusion chromatography (SEC) in respect to poly (methylmethacrylate) standards. PNIPAM86-NTBA14: M_n = 179,400 g/mol; D = 4.5; PNIPAM68-NTBA32: M_n = 205,400 g/mol; D = 2.7. SEC of temperature-responsive copolymers was performed using an Ultimate 3000 ThermoFisher Scientific chromatographic complex equipped with PLgel precolumn guard (size 7.5 × 50 mm, particle size 5 μm, Agilent, Ireland) and PLgel MIXED-C column (size 7.5 × 300 mm, particle size 5 μm, Agilent, Ireland) thermostated at 50 °C. The elution was performed in the isocratic mode with dimethylformamide (HPLC isocratic grade, Carlo Erba, Spain) containing 0.10 M LiBr (99+ %, for analysis, anhydrous, Acros Organic, ThermoFisher Scientific, Ireland) at a flow rate of 1 ml/min. SEC traces were recorded on the refractive index detector at 40 °C. The molecular weight characteristics of the polymers were calculated using Chromeleon 7.0 program (Dionex™, ThermoFisher Scientific, Germany) based on poly (methylmethacrylate) standards (EasiCal™, Agilent, Ireland) with Mw/Mn ≤ 1.05.1H NMR (500 MHz) spectra were recorded in deuterated chloroform at 25 °C on a Bruker (UK) AC-500 spectrometer calibrated relative to the residual solvent resonance.

2.3. Fabrication of electrospun scaffolds

Typical protocols for electrospinning were utilised [58,59]. Briefly, 150 mg/ml of PNIPAM86-NTBA14 and PNIPAM68-NTBA32 were dissolved in methanol (Honeywell, Ireland) and the solution was extruded at 20 μl/min through an 18 G stainless steel blunt needle (EDF Nordson, Ireland). Upon application of high voltage (20 kV) between the needle and the aluminium collector (20 cm distance), the solvent evaporated and the electrospun fibres were collected on a rotating (50 revolutions per min) mandrel. All electrospinning experiments were carried out at room temperature (22 °C–26 °C) and 40–55% relative humidity.

2.4. Electrospun scaffold fibre morphology analysis

The electrospun scaffolds were mounted onto carbon disks, gold sputter coated and imaged with a Hitachi S-4700 scanning electron microscope (Hitachi High-Technologies Europe GmbH, Germany). Fibre diameter analysis was conducted using the ImageJ software (NIH, USA).

2.5. Electrospun scaffold stability and swelling analyses

The stability and swelling properties of the electrospun scaffolds were investigated using square samples (2 cm × 2 cm). For stability analysis, each sample was submerged in phosphate buffered saline (PBS) at 37 °C and after 1 h, images were taken using a digital camera (iPhone 6, USA). For swelling analysis, each sample was weighed and then submerged in PBS at 37 °C to allow water uptake. At time intervals of 3, 6, 24, 48 and 72 h, specimens were removed from PBS and prior to weighing of the samples, the excess PBS was removed with tissue paper. The swelling ratio was calculated using the following formula: Swelling Ratio % (S) = [(Ww – Wd)/Wd] x 100, where W_w stands for wet weight and W_d stands for dry weight of the samples.

2.6. Electrospun scaffold contact angle analysis

Sessile-drop experiments were performed with a contact-angle measuring system (Acam D-2, Apex Instruments, India). During the entire test period, the samples were placed on a heated platform with moisture content level maintained at 70%. Deionised water was dropped onto the sample surface from a micro-syringe needle (volume: 10 μl, dispensing rate:15 μl/min). Droplet pictures were taken after the drop touched the sample with a periodicity of 5 s for 15 min. The contact angles were calculated by the instrument's software through analysing the shape of the drop by the tangent fitting method.

2.7. Cell culture

The scaffolds were cut and fixed to the bottoms of 24-well cell culture plate using silicone O-rings. The sterilisation was conducted under UV light for 2 h. Human adipose derived stem cells (hADSCs, RoosterBio, USA) were cultured in alpha-Minimum Essential Medium (α-MEM) with Gibco® GlutaMAX™ (ThermoFisher Scientific, Ireland) supplemented with 10% foetal bovine serum (FBS) and 1% penicillin/streptomycin (P/S) at 37 °C in a humidified atmosphere of 5% CO_2. At passage 3–5, cells were seeded at 25,000 cells/cm^2 in 24 well plates and at 50,000 cells/cm^2 on the temperature-responsive electrospun scaffolds and were allowed to attach. After 24 h, the media were changed to media without/with MMC (carrageenan at 50 μg/ml). Supplementation with 100 μM of L-ascorbic acid 2-phosphate sesquimagnesium salt hydrate was used to induce collagen synthesis. Media were changed every 3 days. Samples were analysed at days 4, 7 and 10.

2.8. Phase contrast microscopy analysis

Phase contrast images were obtained using an inverted microscope (Leica Microsystems, Germany) at each timepoint. Images were processed using ImageJ software (NIH, USA).

2.9. Cell morphology analysis

At each timepoint, cells were fixed with 4% paraformaldehyde, permeabilised with 0.2% Triton X-100 and stained with FITC-labelled phalloidin (ThermoFisher Scientific, UK) for the cytoskeleton and Hoechst for the nucleus. Samples were imaged in an inverted fluorescence microscope (Olympus IX81, Olympus Corporation, Japan).

2.10. Cell viability analysis

At each timepoint, cells were washed with PBS and a solution of Calcein AM (4 mM, ThermoFisher Scientific, UK) and ethidium homodimer I (2 mM, ThermoFisher Scientific, UK) was added. Cells were incubated at 37 °C and 5% CO_2 for 30 min after which, fluorescence images were obtained with an Olympus IX-81 inverted fluorescence microscope (Olympus Corporation, Japan).

2.11. Cell metabolic activity analysis

The alamarBlue® assay (Invitrogen, USA) was used to quantify cell metabolic activity as per manufacturer's protocol. Briefly, at each timepoint, cells were washed with PBS and alamarBlue® solution (10% alamarBlue® in PBS) was added. After 4 h of incubation at 37 °C, absorbance was measured at excitation wavelength of 550 nm and emission wavelength of 595 nm using a Varioskan Flash spectral scanning multimode reader (ThermoFisher Scientific, UK). Cell metabolic activity was expressed as % reduction of the alamarBlue® and normalised to non-MMC control group.

2.12. DNA quantification analysis

DNA quantification was assessed using the Quant-iT™ PicoGreen® dSDNA assay kit (Invitrogen, Ireland) according to the manufacturer's protocol. Briefly, DNA was extracted using a papain extraction reagent for 3 h at 65 °C. 28.7 μl were then transferred into 96-well plates. A standard curve was generated using 0, 100, 200, 375, 500, 1,000, 2000 and 4000 ng/ml DNA concentrations. 71.3 μl of a 1:200 dilution of Quant-iT™ PicoGreen® reagent were added to each sample and the plate was read using a using a Varioskan Flash spectral scanning multimode reader (ThermoFisher Scientific, UK) with an excitation wavelength of 480 nm and an emission wavelength of 525 nm.

2.13. Cell sheet detachment analysis

At each timepoint, electrospun scaffolds with cells were rinsed with pre-warmed PBS. To induce detachment cold PBS (4 °C) was added and samples were left on a digitally controlled chilling/heating dry bath (Torrey Pines Scientific, USA) set to 4 °C. Additional washes with cold PBS were repeated in order to remove any excess of polymer.

2.14. Time lapse microscopy analysis

A Linkam THMS600 Heating and Freezing microscope stage (Linkam Scientific Instruments, UK) was attached to a BX51 Olympus microscope (Olympus Corporation, Japan). Cell detachment was conducted as described above. Images were taken every 5 s until full dissolution of the electrospun scaffolds.

2.15. Sodium dodecyl sulphate-polyacrylamide gel electrophoresis (SDS-PAGE) analysis

SDS-PAGE was conducted as has been described previously [60]. Briefly, at each timepoint cell layers were digested with pepsin from porcine gastric mucosa at 0.1 mg/ml in 0.5 M acetic acid for 2 h at 37 °C with continuous shaking and subsequent neutralisation with 1 N NaOH. The samples for SDS-PAGE were prepared using appropriate dilution with distilled water and 5x sample buffer. 10 μl per sample solution per well were loaded on the gel (5% running gel/3% stacking gel) after 5 min heating at 95 °C. Electrophoresis was performed with a Mini-PROTEAN Tetra Electrophoresis System (Bio-Rad, Ireland) by applying a potential difference of 50 mV for the initial 30 min and 120 mV for the remaining time (approximately 1 h). The gels were stained using a silver stain kit (SilverQuest™, Invitrogen, Ireland) according to the manufacturer's protocol. Images of the gels were taken after brief washing with water. To quantify the cell-produced collagen type I deposition, the relative densities of collagen α1(I) and α2(I) chains were evaluated with ImageJ software (NIH, USA) and compared to the α1(I) and α2(I) chain bands densities of standard collagen type I (Symatese Biomateriaux, France).

2.16. Histological analysis

At each timepoint, the cell sheets were detached from the electrospun scaffolds, fixed in 4% paraformaldehyde for 24 h, washed with PBS, infiltrated with 15% sucrose in PBS for 12 h and in 30% sucrose in PBS overnight and embedded in Tissue Freezing Medium® (Leica Biosystems, Ireland). Subsequently, transverse cryosections of 5 μm in thickness were obtained using the CM1850 Cryostat (Leica Biosystems, Ireland). The samples were then stained with haematoxylin-eosin, Masson-Goldner's trichrome stain (Carl Roth, Germany), Herovici's polychrome stain and Picrosirius red stain according to the manufacturer's guidelines and mounted using DPX mountant. Images were captured with an Olympus IX-81 inverted microscope (Olympus Corporation, Tokyo, Japan). Cell sheet thicknesses were measured using the digitalised images and ImageJ software (NIH, USA). The same staining

protocols were applied for hADSCs grown in 2D culture on glass coverslips as control.

2.17. Immunocytochemistry analysis

At each timepoint, cells were briefly washed with PBS and fixed with 4% paraformaldehyde for 20 min at room temperature. Cells were washed again and non-specific binding sites were blocked with 3% bovine serum albumin (BSA) in PBS for 30 min. The cells were incubated overnight at 4 °C with one of the following primary antibodies: mouse anti-collagen type I, rabbit anti-collagen type III, rabbit anti-collagen type V and rabbit anti-fibronectin. Details of antibodies used for immunocytochemistry are provided in Supplementary Table S1. After 3 washes in PBS, cells were incubated for 30 min at room temperature with the secondary antibody AlexaFluor® 488 goat anti-rabbit (Invitrogen, USA). The cell nuclei were stained with Hoechst. Images were taken with an Olympus IX-81 inverted fluorescence microscope (Olympus Corporation, Japan). The same staining protocol was applied on cryosections, which were mounted with Fluoromount™ Aqueous Mounting Medium and left for 2 h at room temperature to dry before imaging.

2.18. Atomic force microscopy (AFM) analysis

AFM analysis was performed as per previously published protocol [61]. Briefly, freshly cut 5 μm thick sections were attached directly onto 13 mm diameter glass coverslips. Prior to imaging, the sections were thawed, air-dried, washed with water to remove the support medium and air-dried again. Samples were imaged by intermittent contact mode in air using a Dimension 3100 AFM (Veeco, UK) with a Nanoscope IIIa controller and a 12 μm × 12 μm × 3.2 μm (X, Y, Z dimension) E scanner. Height, amplitude and phase images at scan sizes of 1 μm or 5 μm were captured at an initial scan rate of 1.97 Hz and integral and proportional gain settings of 0.3 and 0.5, respectively.

2.19. Trilineage differentiation analysis

For all differentiation experiments cells at passage 5 were seeded at a density of 50,000 cells/cm^2. Osteogenic, adipogenic and chondrogenic assays were performed without (−) or with (+) MMC in the differentiation media. Osteogenic, adipogenic and chondrogenic differentiations were initiated 24 h after seeding and cells were differentiated for 21 days. As control, cells were grown on tissue culture plastic (TCP) for osteogenic and adipogenic differentiation and as pellets for chondrogenic differentiation.

Osteogenesis was induced using media composed of α-MEM with Gibco® GlutaMAX™ (ThermoFisher Scientific, Ireland) supplemented with 10% FBS, 1% P/S, 50 μM L-ascorbic acid 2-phosphate sesquimagnesium salt hydrate, 10 mM β-glycerophosphate, 100 μM dexamethasone, with or without MMC.

Adipogenesis was induced through cycles by 7 days of induction media composed of Dulbecco's modified Eagle medium high glucose (DMEM-HG), supplemented with 10% FBS, 1% P/S, 1 μM rosiglitazone, 1 μM dexamethasone, 0.5 mM 3-isobutyl-1-methylxanthine, 10 μg/ml insulin, with or without MMC and subsequently with maintenance media composed of DMEM-HG, supplemented with 10% FBS, 1% P/S and 10 μg/ml insulin, with or without MMC.

Chondrogenesis was induced using media composed of DMEM-HG, supplemented with 10 ng/ml transforming growth factor β3 (PromoCell GmbH, Germany), 100 nM dexamethasone, 10% insulin-transferrin-selenium, 40 μg/ml L-proline, 100 μM L-ascorbic acid 2-phosphate sesquimagnesium salt hydrate, with or without MMC.

2.20. Alizarin red staining analysis

Samples were fixed with ice-cold methanol for 20 min, stained with 2% alizarin red in deionised water for 10 min and washed with water. Images were acquired using an inverted microscope (Leica Microsystems, Germany). Semi-quantitative analysis of alizarin red staining was performed by dissolving the bound stain with 10% acetic acid. Samples were collected using a cell scraper and heated to 85 °C for 10 min. Subsequently 10% solution of ammonium hydroxide was used to achieve a pH of 4.5. Finally, the absorbance was read at 405 nm using a micro-plate reader (Varioskan Flash, ThermoFisher Scientific, Ireland).

2.21. Oil red O staining analysis

Samples were fixed for 20 min with 4% paraformaldehyde, stained for 10 min with oil red O solution (oil red O 0.5% in isopropanol, diluted 3:2 in distilled water) at room temperature and images were acquired using an inverted microscope (Leica Microsystems, Germany). For quantification of oil red O staining, the dye was extracted pipetting 100% isopropanol over the surface of the wells. Then, the solution was centrifuged at 500×*g* for 2 min to remove debris and the absorbance was measured at 520 nm using a Varioskan Flash spectral scanning multimode reader (ThermoFisher Scientific, Ireland).

2.22. Sulphated glycosaminoglycan analysis

Cell layers and culture media were digested for 3 h at 60 °C with 0.1% crystallised papain in 0.2 M sodium phosphate buffer at pH 6.4, containing sodium acetate, ethylenediaminetetraacetic acid (EDTA), disodium salt and cysteine-HCl. For sulphated glycosaminoglycan (sGAG) quantification, the Blyscan™ Glycosaminoglycan Assay (Biocolor, UK) was used, as per manufacturer's protocol.

2.23. Growth factors and matrix metalloproteinases analysis

The expression of growth factors from conditioned media and cell layers of hADSCs cultured both on TCP and PNIPAM86-NTBA14 without and with MMC and the expression of matrix metalloproteinases (MMPs) from conditioned media and cell layers of hADSCs cultured on PNIPAM86-NTBA14 without and with MMC were assessed using antibody arrays (Abcam, UK), following the manufacturer's protocol (the selected growth factor and MMP involvement in wound healing is listed in Supplementary Table S2 and Supplementary Table S3, respectively). Briefly, hADSCs were cultured for 10 days without and with MMC. For the protein extraction from the cell layers, radioimmunoprecipitation assay buffer with proteinase and phosphatase inhibitor cocktail was added to the cell layers and left to incubate at 4 °C for 30 min, after which cell layers were scratching collected, centrifuged and frozen at −80 °C. 6 replicates were pooled prior to total protein quantification, which was performed using the Pierce™ BCA Protein Assay Kit (ThermoFisher Scientific, UK) following the manufacturer's protocol. Protein concentration was determined using a BSA standard curve. For the conditioned media, at day 10, the culture media was removed and replaced with fresh media containing 0.2% FBS, which was subsequently collected after 3 days. 6 replicates were pooled prior to analysis. The antibody membranes were incubated overnight with 1 ml of conditioned media or 250 μg of proteins. The array membranes were developed using an enhanced chemiluminescence method according to the manufacturer's protocol. The relative expression of the growth factors and the MMPs was determined by measuring the pixel intensity of each chemiluminescence image.

2.24. Scratch and migration assays analysis

To analyse the effect of MMC on cell migration, a scratch wound healing assay [62] and a migration assay [63] were performed. For the scratch assay, hADSCs were cultured for 10 days with and without MMC. Before starting the assay, cells were serum starve for 16 h with media containing 0.2% FBS. Two perpendicular scratches were created with a

P10 pipette tip. To remove detached cells and proteins after wound creation, cells were rinsed once with PBS and new media containing 0.2% FBS was added. Images were obtained at 0, 24, 48 and 72 h. The migration assay was performed using a 2 well silicone insert with a defined cell-free gap (IBIDI, Germany). Values were reported as percent of wound closure and calculated as follows: [(area of original wound/gap – area of actual wound/gap)/area of original wound/gap] x 100.

2.25. Mouse excisional wound splinting model

All animal experiments and procedures were conducted in accordance to Irish laws on animal experimentation and were approved by the Animal Care and Research Ethics Committee of NUI Galway and the Irish Health Products Regulatory Authority (Licence Number: AE 19125/P051). A total of 18 female athymic nude mice (6–7 weeks old), purchased from Charles River (UK), were included in the study. The mice were kept in individually ventilated cages with controlled temperature and humidity and a 12 h light-dark cycle. All animals were housed in groups prior to surgery and were provided access to food and water *ad libitum*. Postoperatively, the animals were housed individually to avoid chewing of wounds and bandages. After one-week acclimatisation period, animals were randomly divided into the following three groups: non-treated control (n = 6), cell sheets without MMC (-MMC, n = 6) and cell sheets with MMC (+MMC, n = 6). Every animal received perioperative analgesia with a subcutaneous injection of buprenorphine (0.05 mg/kg, Bupaq®, Chanelle Pharma Group, Ireland) 1 h prior to surgical anaesthesia. Anaesthesia was induced and maintained with isoflurane (Iso-Vet®, Chanelle Pharma Group, Ireland). A splinted wound healing model was utilised [64]. Briefly, the surgical field at the back of each mouse was cleaned with iodine scrub and 70% ethanol solution. The skin was folded and two circular full thickness (epidermis, dermis, subcutaneous tissue and panniculus carnosus muscle) wounds of 5 mm diameter were created with a single puncture using a punch biopsy (KAI Medical, Italy). A silicone splint with internal and external diameter of 6 mm and 12 mm, respectively, and 0.5 mm thickness (Grace Bio-Labs, USA) was sutured around every wound to prevent contraction and promote healing by epithelisation. An identical treatment was applied to both wounds of each mouse. Animals received twice per day a subcutaneous injection of buprenorphine (0.05 mg/kg) for post-operative analgesia and once per day a subcutaneous injection of enrofloxacin (5 mg/kg, Baytril®, Bayer, Germany) as antibiotic treatment for 3 days.

2.26. Cell labelling and in vivo cell tracking analysis

Before implantation, cell sheets were incubated with 10 μM Vybrant™ DiD fluorescent dye (ThermoFisher Scientific, Ireland) overnight at 37 °C and then washed 3 times for 5 min each with sterile PBS. Before imaging, animals were anesthetised with isoflurane. The wavelengths of absorption were set up at 644 nm excitation and 665 nm emission. Digital pictures of animals were taken immediately post-surgery and at days 3, 7, 10 and 14 with the Spectrum In Vivo Imaging System IVIS® Lumina III (PerkinElmer, UK). Average radiant efficiency was calculated with Living Image Software® (IVIS Imaging Systems, UK).

2.27. Wound healing ratio analysis

Wound closure rate was determined by taking digital pictures of the wounds with an iPad Pro (Apple, USA) immediately post-surgery and at days 3, 7, 10 and 14. The planimetric area of the open wounds was measured using the software WoundWise IQ (Med-Compliance IQ, USA). Values were reported as % of wound closure and calculated as follows: [(area of original wound – area of actual wound)/area of original wound] x 100.

2.28. Histological analysis

After euthanasia, skin tissue samples were harvested and fixed in 4% paraformaldehyde for paraffin embedding. 5 μm in thickness cross-sections were prepared from all paraffin blocks. The sections were deparaffinised with 2 immersions in xylene and re-hydrated with descending concentrations of ethanol (100%, 90%, 70%, 0% in distilled water). Sections were stained using haematoxylin-eosin, Masson-Goldner's trichrome stain (Carl Roth, Germany), Herovici's polychrome stain and Picrosirius red according to the manufacturer's protocols and mounted using DPX mountant. Slides were scanned and images were captured using an Olympus VS120 virtual slide microscope and OlyVIA software and an Olympus BX51 microscope for polarised microscopy analysis (all Olympus Corporation, Japan).

2.29. Immunohistochemistry analysis

Paraffin sections were dewaxed and re-hydrated as described above. Endogenous peroxidases were blocked by incubating the samples in 3% hydrogen peroxide in 100% methanol for 20 min. Antigen retrieval was carried out in a pressure cooker in 0.01 M Tris-EDTA (pH 9.0). The slides were then incubated for 30 min at room temperature in antigen blocking solution (5% normal goat serum and 0.1% Triton X-100 in PBS). Slides were incubated overnight at 4 °C with the following primary antibodies: rabbit *anti*-cytokeratin 5, rabbit anti-CD 31 and mouse anti-human nuclear antigen. Details of antibodies used for immunocytochemistry are provided in Supplementary Table S1. Secondary antibodies, biotinylated swine anti-rabbit and biotinylated rabbit anti-mouse (Dako, USA), were added and the slides were further incubated for 1 h at room temperature. For the detection, ABC horseradish peroxidase labelled Vectastain Elite ABC reagent (Vector, UK) was used. Binding sites of primary antibodies were visualised using diaminobenzidine (Dako, UK) as chromogen and all sections were counterstained with haematoxylin. Negative controls were prepared for each stain by omitting primary antibodies during incubation, which resulted in no staining. Human skin tissue sections were used as positive controls for anti-human nuclear antigen antibody. Images were captured using an Olympus VS120 digital scanner and OlyVIA software (both Olympus Corporation, Japan).

2.30. Epidermal thickness analysis

The thickness of the neo-formed epidermis was evaluated with ImageJ (NIH, USA) using Masson-Goldner's trichrome stained histological sections. Beginning from the centre of the wound, 3 non-consecutive sections (100 μm distance from each another) per group, were analysed by randomly selecting 3 high-power fields and performing 5 measurements of the epidermal thickness per field.

2.31. Scar size analysis

Scar size analysis was performed as per established protocols [65]. Briefly, scar area was evaluated using Masson-Goldner's trichrome stained histological sections. Beginning from the centre of the wound, 3 non-consecutive sections per group, with a distance of 100 μm, were analysed by randomly selecting 3 high-power fields and performing 5 measurements of the scar size per field. Scar tissue was outlined using the freeform outline tool in ImageJ (NIH, USA) to produce a pixel-based area measurement, which then converted to μm^2. Scar area measurements were performed extended to the panniculus carnosus. A positive and predictive relationship was established between dermal thickness and scar area. Scar size was determined by the scar index, which was calculated as follow: scar index (μm) = scar area (μm^2)/average dermal thickness (μm). Dermal thickness measurements were obtained using ImageJ (NIH, USA) by drawing a line normal to the average orientation of the epidermal-dermal and dermal-subcutaneous tissue demarcations. 4 dermal thickness measurements were taken per sample, two adjacent

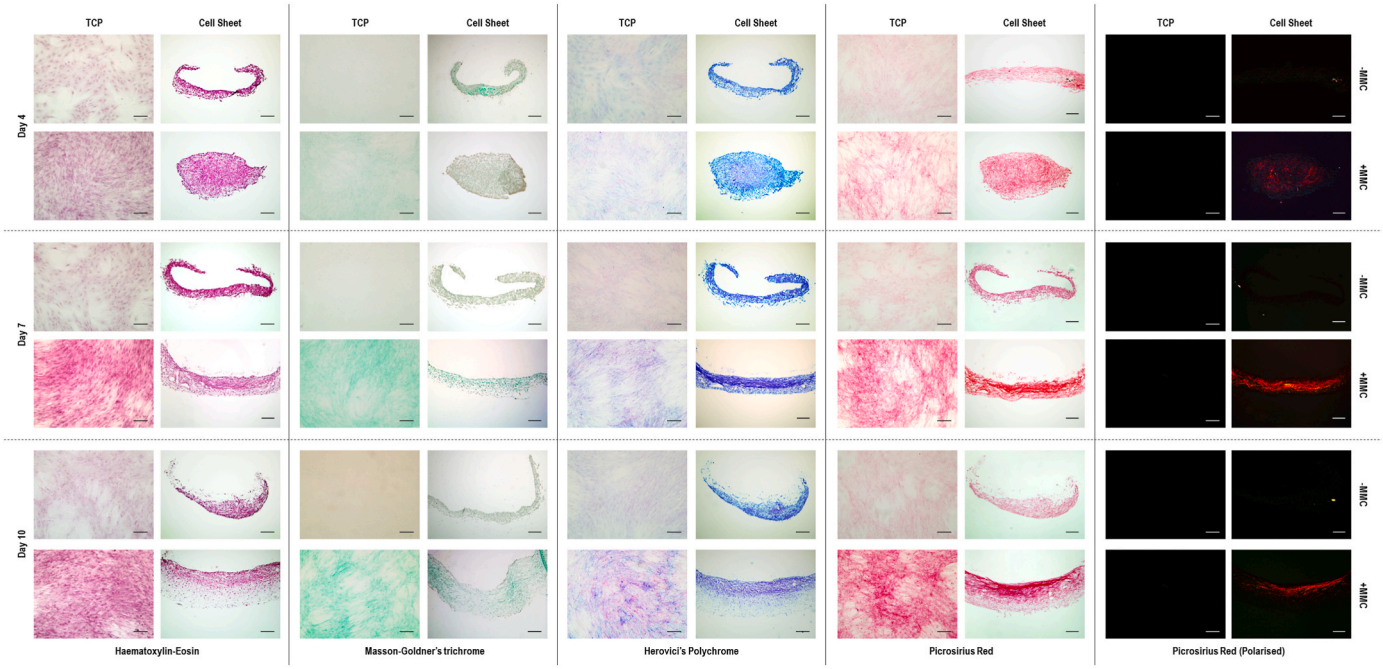

Fig. 1. Histological analysis of hADSCs grown without (−) and with (+) MMC on two-dimensional TCP revealed that MMC increased ECM deposition (pink in haematoxylin-eosin), which was primarily collagenous (green in Masson-Goldner's trichrome and bright red in Picrosirius red) and was maturing as a function of time in culture (young collagen blue and mature collagen pink to red in Herovici's polychrome), but did not improve structural order (no signal in polarised microscopy). Histological analysis of hADSCs grown without (−) and with (+) MMC on three-dimensional temperature-responsive electrospun scaffolds (the samples were obtained after dissolving the scaffolds by switching the temperature) revealed similar results, but now MMC allowed the development of a three-dimensional tissue-like structure and, importantly, polarised microscopy (stained bright red) made apparent that MMC induced a high organisational order. Scale bar: 100 μm. N = 3. (For interpretation of the references to color in this figure legend, the reader is referred to the Web version of this article.)

to the wound site at 50 μm on either side, and two at a farther distance of 700 μm on either side of the wound.

2.32. Statistical analysis

Data are expressed as mean ± standard deviation. Number of replicates is indicated in each figure legend. Statistical analysis was performed using MINITAB® version 19 (Minitab Inc, USA). One-way analysis of variance (ANOVA) was used for multiple comparisons and Tukey's post hoc test was used for pairwise comparisons after confirming the samples followed a normal distribution (Anderson-Darling test) and had equal variances (Bartlett's and Levene's test for homogeneity of variances). When either or both assumptions were violated, non-parametric analysis was conducted using Kruskal-Wallis test for multiple comparisons and Mann-Whitney test for pairwise comparisons. Statistical significance was accepted at $p < 0.05$.

3. Results

3.1. Morphology, stability, swelling, contact angle and dissolution analyses of temperature-responsive electrospun scaffolds

Scanning electron microscopy analysis (PNIPAM Supplementary Figure S1A, PNIPAM86-NTBA14 Supplementary Figure S1B, PNIPAM68-NTBA32 Supplementary Figure S1C) revealed that all electrospun scaffolds were composed of uniform (bead-free) randomly oriented fibres. Fibre diameter distribution analysis showed that the PNIPAM scaffolds (Supplementary Figure S1D) were comprised of fibres with diameter range from 300 nm to 600 nm and the PNIPAM86-NTBA14 (Supplementary Figure S1E) and PNIPAM68-NTBA32 (Supplementary Figure S1F) scaffolds were comprised of fibres with diameter range from 1,000 nm to 2,000 nm.

Stability analysis (Supplementary Figure S2A) revealed that the PNIPAM (LCST 32 °C) electrospun scaffolds were completely soluble, whilst the PNIPAM86-NTBA14 (LCST 25 °C) and the PNIPAM68-NTBA32 (LCST 16 °C) electrospun scaffolds were stable in PBS at 37 °C.

Swelling ratio analysis (Supplementary Figure S2B) showed that the PNIPAM86-NTBA14 electrospun scaffolds had swelling ratio of 5% up to 24 h and then increased to 35% until the end of the experiment (72 h) and the swelling ratio of the PNIPAM68-NTBA32 electrospun scaffolds did not exceed the 4% for the duration of the experiment (72 h).

Static contact angle measurements against deionised water (Supplementary Figure S2C) made apparent that the PNIPAM86-NTBA14 electrospun scaffolds had average contact angle of 74° ± 4° and the PNIPAM68-NTBA32 electrospun scaffolds had average contact angle of 81° ± 2°.

Time-lapse microscopy revealed that the PNIPAM86-NTBA14 electrospun scaffolds were dissolved in fast and uniform manner (Supplementary Video S1) and the PNIPAM68-NTBA32 electrospun scaffolds were dissolved slowly in a layer-by-layer fashion (Supplementary Video S2).

3.2. Cell attachment, spreading, viability, DNA concentration, metabolic activity analyses and cell sheet detachment analyses

Qualitative rhodamine-phalloidin staining (Supplementary Figure S3) showed that at all timepoints and without and with MMC the PNIPAM86-NTBA14 and the PNIPAM68-NTBA32 electrospun scaffolds supported hADSC attachment and spreading in similar manner to the control TCP.

Qualitative (Supplementary Figure S4A) and quantitative (Supplementary Figure S4B) hADSC viability analyses revealed no apparent differences ($p > 0.05$) at any timepoint and without and with MMC between the control TCP and the PNIPAM86-NTBA14 and the PNIPAM68-NTBA32 electrospun scaffolds.

Cell sheet detachment from the PNIPAM86-NTBA14 electrospun

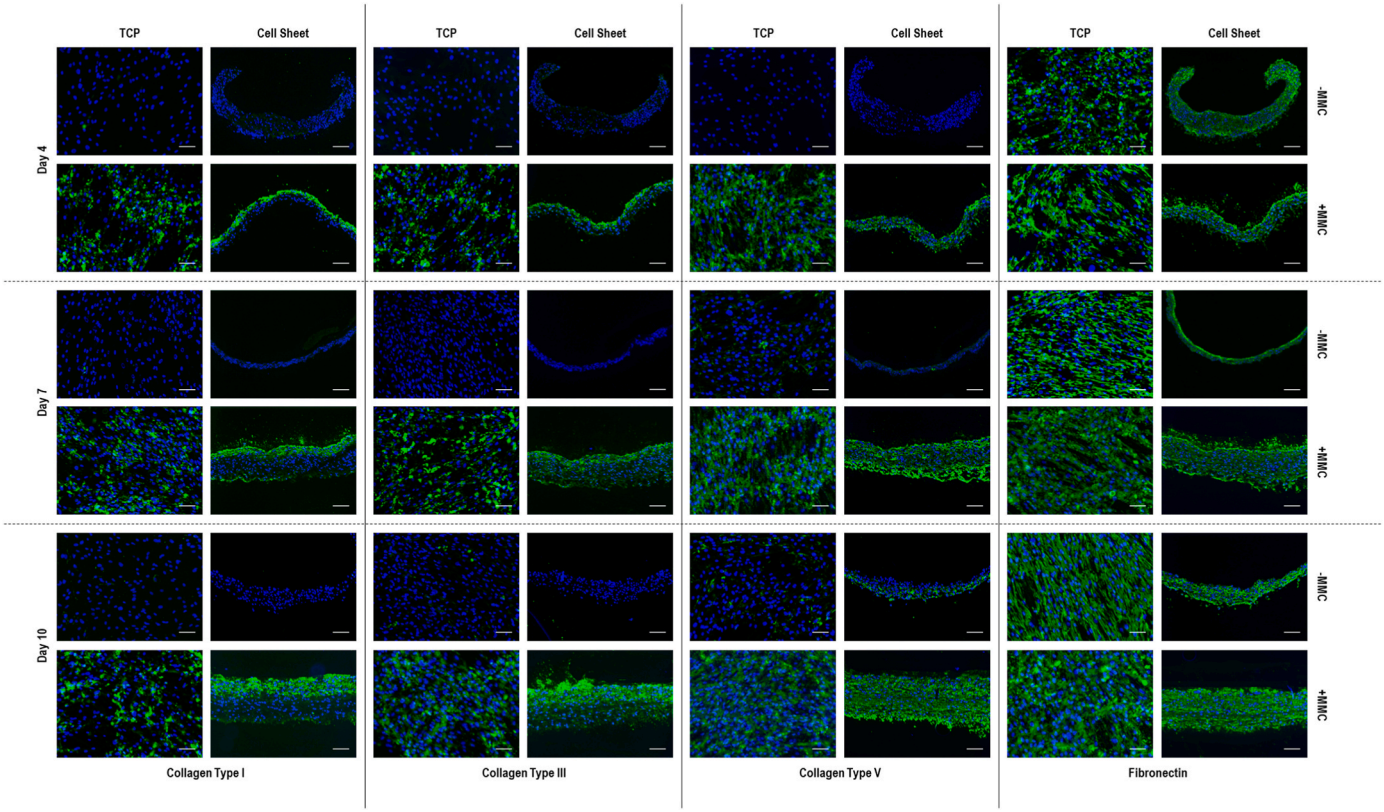

Fig. 2. Immunocytochemistry analysis of hADSCs grown without (−) and with (+) MMC on two-dimensional TCP revealed that MMC increased collagen type I (green), collagen type III (green) and collagen type V (green) deposition, without affecting fibronectin (green) deposition. Histological analysis of hADSCs grown without (−) and with (+) MMC on three-dimensional temperature-responsive electrospun scaffolds (the samples were obtained after dissolving the scaffolds by switching the temperature) revealed similar results, but now MMC allowed the development of a three-dimensional tissue-like structure. Nuclei: blue. Scale bar: 100 μm. N = 3. (For interpretation of the references to color in this figure legend, the reader is referred to the Web version of this article.)

scaffolds ranged from 5 min to 10 min and from the PNIPAM68-NTBA32 electrospun scaffolds ranged from 3 to 4 h (data not shown); for this reason, all subsequent experiments were conducted only with the PNIPAM86-NTBA14 electrospun scaffolds.

Qualitative image analysis (Supplementary Figure S5A) made apparent that intact cell sheets without and with MMC were obtained from the PNIPAM86-NTBA14 electrospun scaffolds at all timepoints and qualitative phase contrast microscopy analysis (Supplementary Figure S5B) showed minimal cell sheet shrinkage after complete detachment.

hADSC DNA concentration (Supplementary Figure S6A) on TCP was not significantly ($p > 0.05$) affected as a function of time in culture and absence or presence of MMC; on PNIPAM86-NTBA14 electrospun scaffolds was significantly ($p < 0.05$) increased as a function of time in culture, but not ($p > 0.05$) as a function of MMC. hADSC metabolic activity (Supplementary Figure S6B) was not significantly ($p > 0.05$) affected as a function of time in culture, absence or presence of MMC and culture substrate (TCP or PNIPAM86-NTBA14 electrospun scaffolds).

3.3. SDS-PAGE, histology, immunocytochemistry and AFM analyses

SDS-PAGE and corresponding densitometric analyses of hADSCs on TCP (Supplementary Figure S7A) and on PNIPAM86-NTBA14 electrospun scaffolds (Supplementary Figure S7B) revealed that MMC significantly ($p < 0.01$) increased collagen type I deposition at all timepoints, which was matured as a function of time in culture, as evidenced by the presence of β- and γ-bands.

Histological analysis (Fig. 1) of hADSCs grown on TCP and on PNIPAM86-NTBA14 electrospun scaffolds revealed abundant ECM deposition in the presence of MMC. In particular, in the case of cell sheets derived from culturing hADSCs on PNIPAM86-NTBA14 electrospun scaffolds, histological analysis (Fig. 1) using haematoxylin-eosin showed that cells assembled into multiple layers, across all timepoints both without and with MMC, with the MMC groups leading to thicker tissue-like assemblies; Masson-Goldner's trichrome verified the presence of a collagen-rich ECM in the MMC groups at all timepoints; Herovici's polychrome and Picrosirius red indicated that the use of MMC resulted in cell sheets with densely packed mature collagen fibres; and polarised microscopy of Picrosirius red stained sections revealed a higher organisational order in the presence of MMC. Quantification of cell sheet thickness and estimation of micro tissue volume in the absence and presence of MMC (Supplementary Table S4) revealed that MMC resulted at day 4, in 2.7 and 3.9, at day 7, 3.4 and 4.4 and at day 10, 2.4 and 5.3-fold increase in thickness and estimated volume in comparison to the non-MMC counterparts.

Immunocytochemistry (Fig. 2) and complementary relative fluorescence intensity (Supplementary Figure S8) analyses made apparent that, in general, at all timepoints MMC significantly ($p < 0.05$) increased collagen type I, collagen type III, collagen type V and fibronectin deposition in hADSC cultures on PNIPAM86-NTBA14 electrospun scaffolds (apart from collagen type III at day 4) and on TCP (apart from collagen type III at day 7 and fibronectin at all timepoints). Further immunocytochemistry analysis of longitudinal sections of the cell sheets (Supplementary Figure S9) revealed a homogenous distribution of the collagen type I, collagen type III, collagen type V and fibronectin.

AFM analysis of hADSCs on PNIPAM86-NTBA14 electrospun scaffolds (Supplementary Figure S10) further corroborated the abundantly deposited ECM when MMC was used and indicated physiological collagen assembly by the ample presence of quarter staggered (D-banded) fibrils.

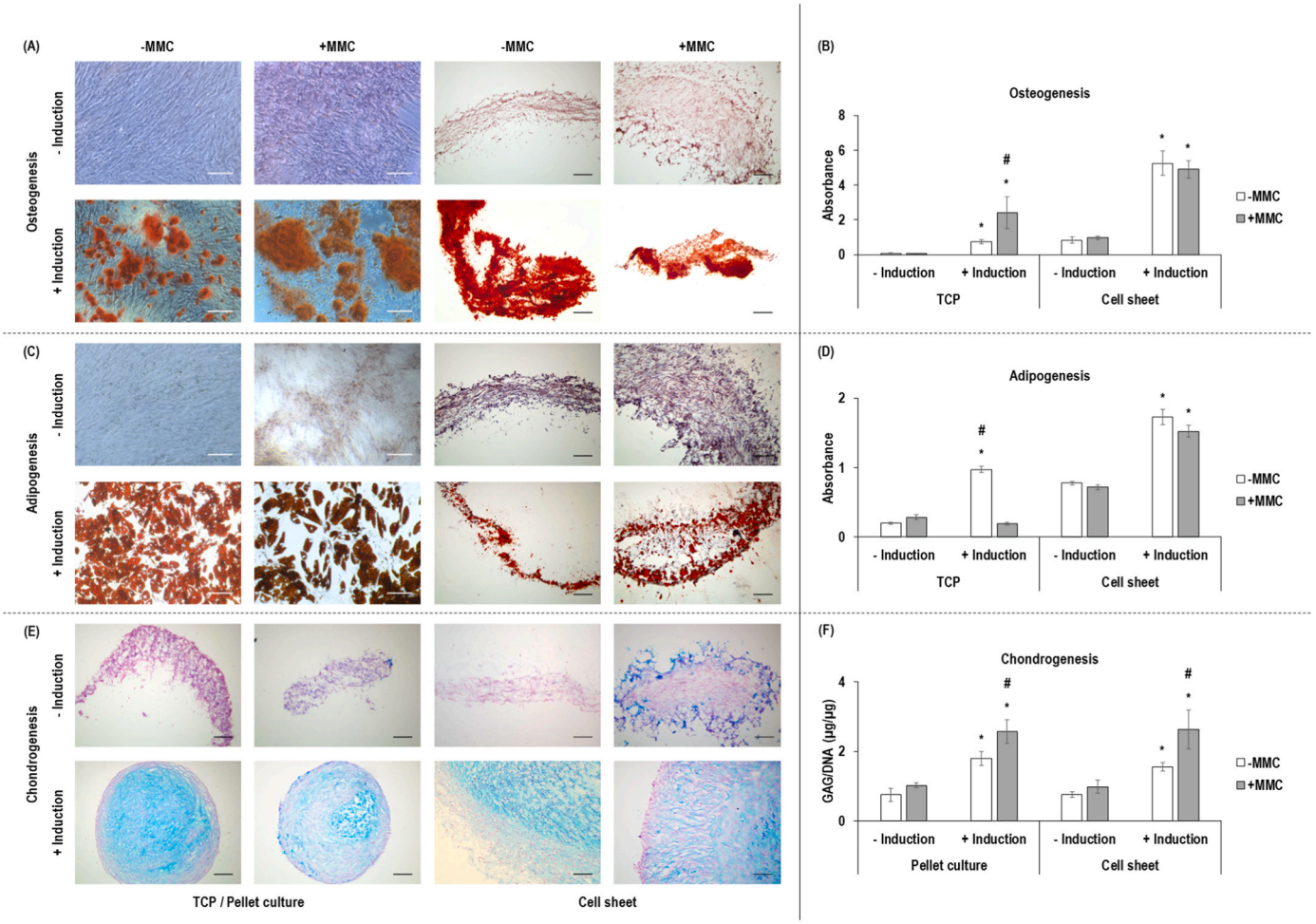

Fig. 3. Osteogenic differentiation (A) and absorbance quantification of Alizarin red staining (B) revealed that MMC induced significantly ($p < 0.05$) higher amounts of calcium nodules of hADSCs grown on two-dimensional TCP, whilst no significant ($p > 0.05$) differences were observed between without (−) and with (+) MMC when hADSCs were grown on three-dimensional temperature-responsive electrospun scaffolds (the samples were obtained after dissolving the scaffolds by switching the temperature). Adipogenic differentiation (C) and absorbance quantification of oil red O staining (D) revealed that MMC significantly ($p < 0.05$) reduced the adipogenic potential of hADSCs grown on two-dimensional TCP, whilst no significant ($p > 0.05$) differences were observed between without (−) and with (+) MMC when hADSCs were grown on three-dimensional temperature-responsive electrospun scaffolds (the samples were obtained after dissolving the scaffolds by switching the temperature). Chondrogenic differentiation (E) and GAG quantification analysis (F) revealed that MMC significantly ($p < 0.05$) increased GAG content of hADSCs that were grown on both three-dimensional pellet culture and three-dimensional temperature-responsive electrospun scaffolds (the samples were obtained after dissolving the scaffolds by switching the temperature). * indicates statistically significant difference to the corresponding -induction control group ($p < 0.05$). # indicates statistically significant difference to -MMC ($p < 0.05$). Scale bar 100 µm. N = 3. (For interpretation of the references to color in this figure legend, the reader is referred to the Web version of this article.)

3.4. Trilineage differentiation analysis

Alizarin red staining (Fig. 3A) and corresponding absorbance quantification (Fig. 3B) revealed that on TCP, the highest ($p < 0.05$) level of osteogenesis was obtained when hADSCs were cultured with differentiation media containing MMC and on PNIPAM86-NTBA14 electrospun scaffolds, osteogenesis was successfully obtained when hADSCs were cultured with osteogenic induction media both without and with MMC [no significant difference ($p > 0.05$) was observed between the -MMC and the +MMC groups during osteogenic induction], as evidenced by the significantly ($p < 0.05$) increase in calcium nodules deposition in comparison to non-differentiated control.

Oil red O staining (Fig. 3C) and corresponding absorbance quantification (Fig. 3D) made apparent that on TCP, the highest ($p < 0.05$) level of adipogenesis was obtained when hADSCs were cultured without MMC during differentiation and on PNIPAM86-NTBA14 electrospun scaffolds, the adipogenesis was successfully obtained when hADSCs were cultured with adipogenic induction media both without and with MMC [no significant difference ($p > 0.05$) was observed between the -MMC and the +MMC groups during adipogenic induction], as evidenced by the significantly ($p < 0.05$) increase in lipid droplets accumulation in comparison to non-differentiated control.

Alcian blue staining (Fig. 3E) and GAG quantification (Fig. 3F) demonstrated that on pellet cultures and on PNIPAM86-NTBA14 electrospun scaffolds, the highest ($p < 0.05$) level of chondrogenesis was obtained when hADSCs were cultured with MMC during chondrogenic induction.

3.5. Growth factors and matrix metalloproteinases analyses

Growth factor antibody array of hADSCs cultured on TCP (array setup: Supplementary Figure S11A, arrays for conditioned media and cell layers: Supplementary Figure S11B) and complementary overall (Supplementary Figure S11C) and ratio between soluble and matrix-bound growth factors (Supplementary Figure S11D) quantification analyses revealed that MMC increased growth factor content in the cell layer.

Growth factor (array setup: Supplementary Figure S12A, arrays for

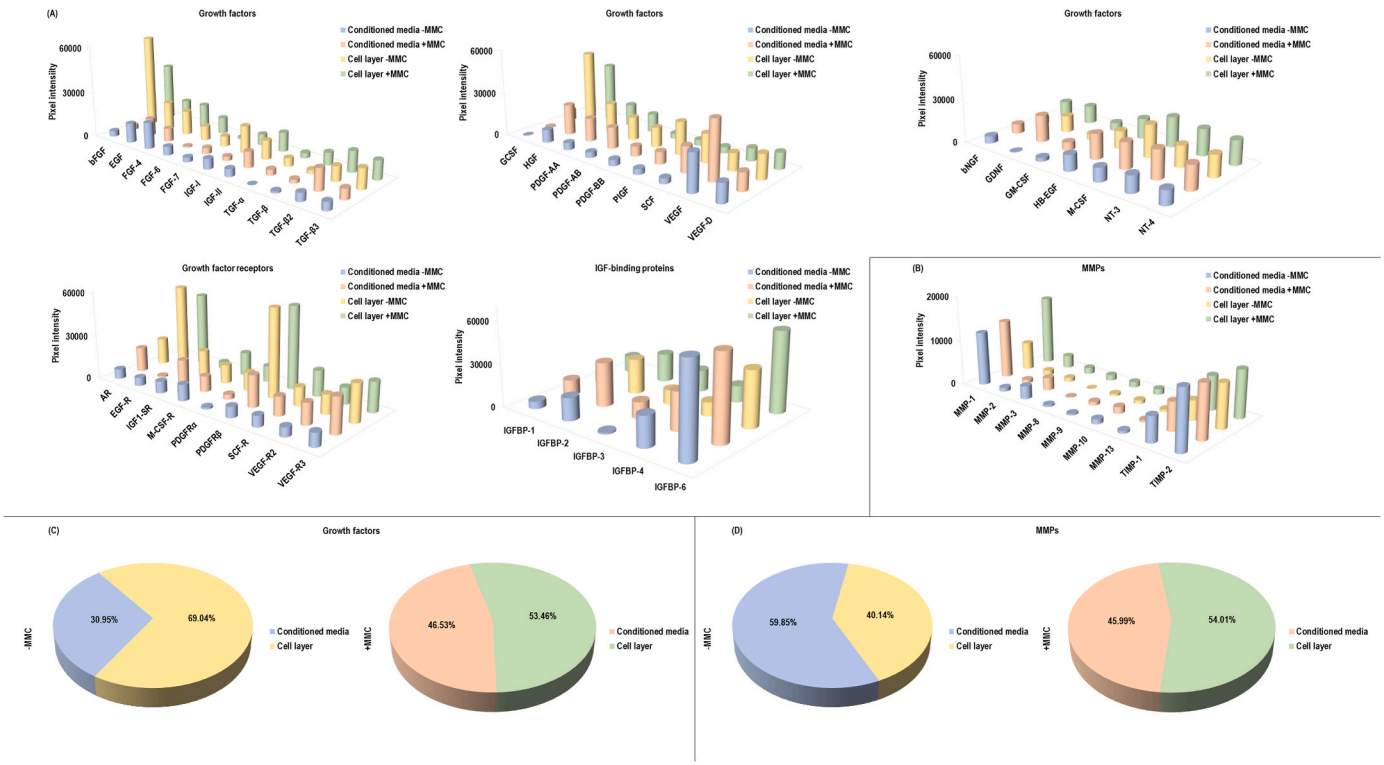

Fig. 4. Growth factor (A) and MMPs (B) antibody array quantification analyses and ratio between soluble and matrix-bound growth factors (C) and MMPs (D) of hADSCs cultured on PNIPAM86-NTBA14 electrospun scaffolds revealed that MMC increased growth factor content in the conditioned media and increased MMP content in the cell layers. N = 1 (6 replicates were pooled in one membrane).

conditioned media and cell layers: Supplementary Figure S12B) and MMP (array setup: Supplementary Figure S13A, arrays for conditioned media and cell layers: Supplementary Figure S13B) antibody array of hADSCs cultured on PNIPAM86-NTBA14 electrospun scaffolds and complementary overall (for growth factors: Fig. 4A, for MMPs: Fig. 4B) and ratio between soluble and matrix-bound growth factors (Fig. 4C) and ratio between soluble and matrix-bound MMPs (Fig. 4D) quantification analyses revealed that MMC increased growth factor content in the conditioned media and increased MMP content in the cell layers.

3.6. Scratch and migration assay analyses

Scratch wound healing assay (Supplementary Figure S14A) and corresponding quantification analysis (Supplementary Figure S14B) in hADSC cultures revealed that MMC induced significantly ($p < 0.05$) faster gap closure within 24 h, whilst in the absence of MMC 48 h were needed. Migration assay (Supplementary Figure S14C) and corresponding quantification analysis (Supplementary Figure S14D) in hADSC cultures made apparent that MMC induced significantly ($p < 0.05$) slower gap closure after 48 h and 72 h than in the absence of MMC.

3.7. Transplantation analysis

In vivo cell tracking (Fig. 5A) and complementary average radiance efficiency (Fig. 5B) analyses revealed that the without and the with MMC groups retained the cells at the implantation site with no apparent differences ($p > 0.05$) between the groups. Qualitative (Fig. 5C) and quantitative (Fig. 5D) wound closure analysis revealed that at day 3, all conditions showed no significant difference ($p > 0.05$) in wound closure capacity; at day 7, the MMC group had the highest ($p < 0.001$) % of wound closure; at day 10, the MMC group had significantly ($p < 0.05$) higher wound closure capacity than the control, but no significant difference ($p > 0.05$) was observed between the control and the non MMC group and the non MMC and the MMC group in wound closure capacity; and at day 14, all conditions reached total wound closure with no significant difference ($p > 0.05$) between them.

Haematoxylin-eosin staining (Fig. 6A) showed complete re-epithelisation in all groups after 14 days. Masson's trichrome staining (Fig. 6B) revealed dense collagenous tissue formation in the cell sheet groups (without and with MMC), but not in the sham group. Herovici's polychrome staining (Fig. 6C) showed that the cell sheet groups, in particular the MMC group, induced a neotissue composed primarily of mature collagen, whilst the sham group formed neodermis primarily composed of immature collagen. Picrosirius red staining (Fig. 6D) and complementary polarised microscopy (Fig. 6E) analyses further corroborated that the cell sheet groups, especially the MMC group, had an ECM mainly composed of densely packed mature collagen fibres, whilst the sham group was composed of a loosely packed immature collagen network.

Immunohistochemical analysis of cytokeratin 5 (Fig. 6F) revealed that in the without and with MMC groups, its expression was evidenced in both epidermal and dermal layers, whilst in the sham group, its expression was restricted only to the epidermal layer and the MMC group appeared to substantially increase the number of hair follicles, in comparison to the without MMC and sham groups. The MMC group, as opposed to the without MMC and the sham groups, appeared to promote neovascularisation, as evidenced by immunohistochemical analysis of CD31 positive cells responsible for new blood vessel formation (Fig. 6G). The cell sheet groups (both without and with MMC) retained the transplanted cells in the wounds up to 14 days (longest timepoint assessed), as evidenced by immunohistochemical staining of human nuclear antigen (Fig. 6H).

Epidermal thickness analysis (Supplementary Figure S15A) revealed no statistically significant differences ($p > 0.05$) between the groups and scar index analysis (Supplementary Figure S15B) indicated that the MMC group induced the lowest ($p < 0.05$) scar index.

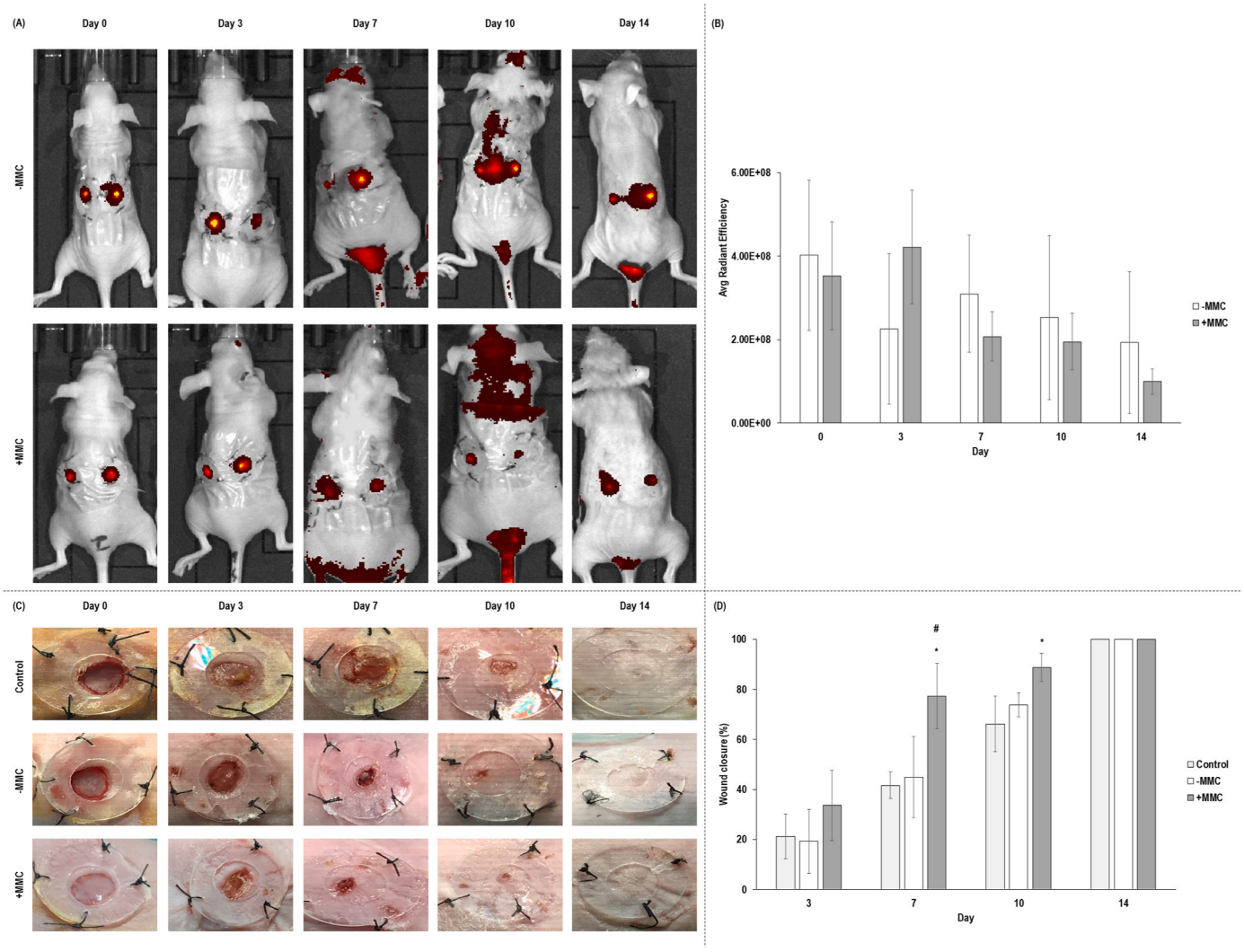

Fig. 5. *In vivo* cell tracking (A) and complementary average radiance efficiency analysis (B) revealed no significant ($p > 0.05$) differences in hADSC retention at the site of implantation between the without (−) and with (+) MMC groups. Qualitative (C) and quantitative (D) wound closure analysis revealed that at day 7 and day 10, the MMC group induced the highest ($p < 0.001$) % of wound closure. * indicates statistically significant difference to the control group ($p < 0.001$). # indicates statistically significant difference to -MMC group ($p < 0.001$). N = 6 for both experiments.

4. Discussion

Scaffold-free tissue engineering aspires to develop 3D tissue surrogates capitalising on the inherent capacity of cells to build tissues and organs. Despite the significant strides that have been achieved over the years and the positive (with respect to both safety and efficacy) preclinical and clinical data, issues associated with very high cell number required that is frequently not available in autologous therapies and the time required to develop a 3D implantable device that not only associated the cell to phenotypic drift, but also the produced device is not really 3D, have jeopardised their wide acceptance and commercialisation. Considering that MMC has been shown to dramatically accelerate ECM deposition in eukaryotic cell culture and to control cell fate during *in vitro* culture, herein, we ventured to assess whether MMC coupled with a temperature-responsive electrospun scaffold can develop safe and functional 3D tissue equivalents using only a fraction of cells and time that conventional scaffold-free approaches utilise.

Starting with the scaffold fabrication element of this work, we demonstrated that the use of the hydrophobic NTBA monomer, at an optimal ratio of 14%, not only decreased the phase transition temperature of the PNIPAM-based electrospun scaffold, but also decreased its response to temperature shift, being stable in wet state, without jeopardising cell attachment and basic cellular functions, as it has been previously demonstrated for PNIPAM-NTBA temperature-responsive films [66,67]. It is also worth noting that commercially available PNIPAM-based temperature-responsive dishes need relatively long time to detach cell sheets (30–60 min) [68,69], which rapidly fold and shrink, requiring substantial infrastructure investment for cell sheet manipulation and transplantation [70,71] and the enhanced ECM deposition (due to MMC), prohibits the release of intact ECM-rich cell layers [47,48]. Herein, not only we fabricated for first time PNIPAM-NTBA electrospun scaffolds, but we also demonstrated that the produced scaffolds, with a simple temperature shift (from 37 °C to 4 °C), allowed fast (5–10 min), detachment of intact cell sheets without shrinkage, even in the presence of abundant ECM (due to MMC).

Moving into the scaffold-free device development and characterisation, MMC maintained physiological cell function, as judged by basic cell function, growth factor, MMP, SDS-PAGE, immunocytochemistry and histological analyses, as has been shown before for various permanently differentiated [35,38] and stem [38,51] cell populations. The significance of this work lays on the fact that using only 50,000 cells/cm^2 and 10 days of MMC culture time, we developed in one step process a living substitute of more than 300 μm in thickness. To substantiate this, one should consider that traditional

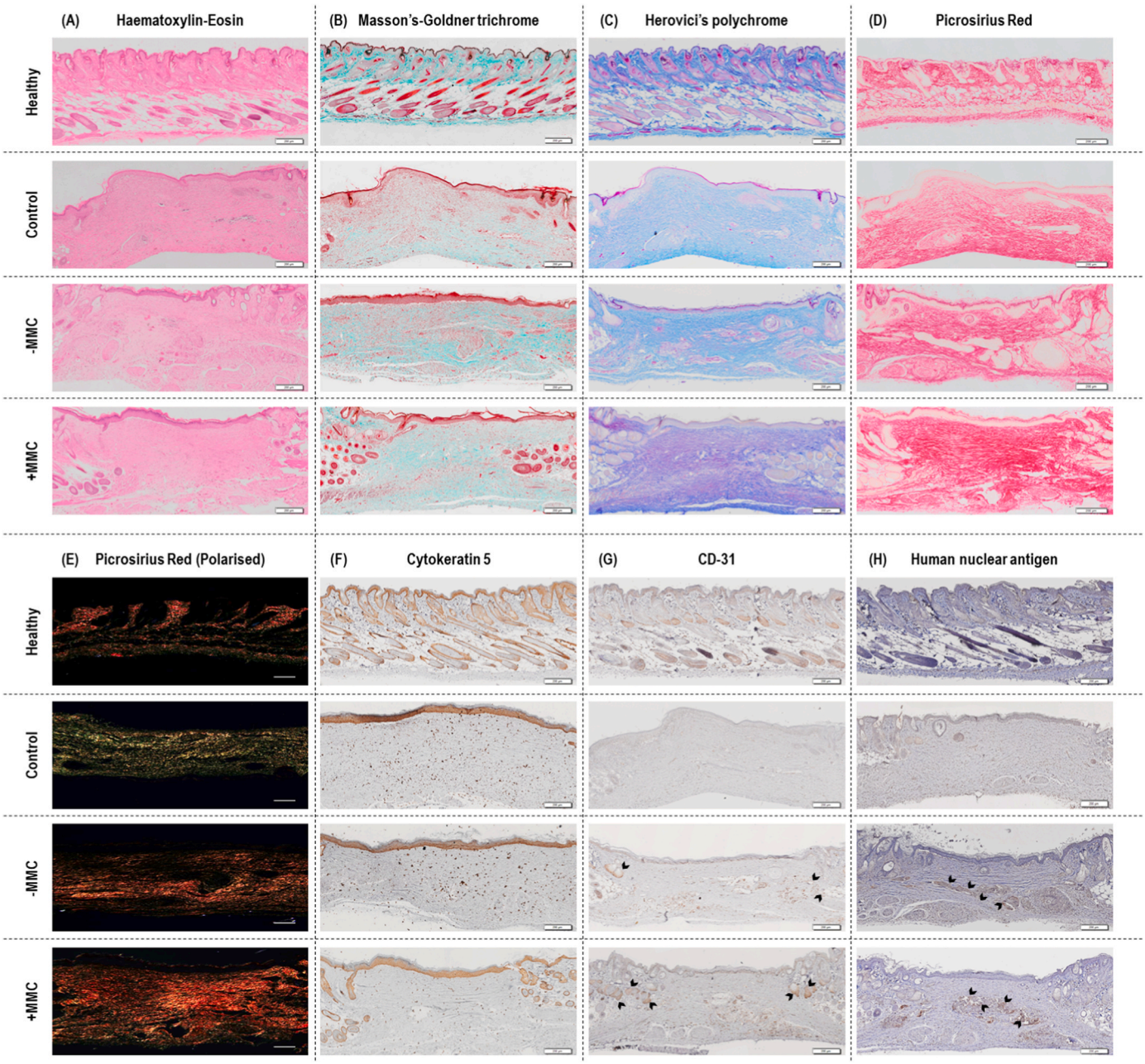

Fig. 6. (A) Haematoxylin-eosin staining showed complete re-epithelisation in all groups. (B) Masson-Goldner's trichrome staining revealed dense collagenous tissue formation in the without (−) and with (+) MMC groups, but not in the control group. (C) Herovici's polychrome staining showed that the without (−) and, in particular, the with (+) MMC groups formed neotissue composed of mature collagen, whilst the control group formed neotissue composed of immature collagen. (D) Picrosirius red staining and (E) complementary polarised microscopy revealed that the without (−) and, in particular, the with (+) MMC groups formed neotissue with ECM mainly composed of densely packed mature collagen fibres, whilst the control group formed neotissue mainly composed of loosely packed immature collagen network. (F) Immunohistochemical analysis of cytokeratin 5 showed increased number of hair follicles in the +MMC group in comparison to the -MMC and control groups. (G) Immunohistochemical analysis of CD31 positive cells showed the presence of a higher number of neo-formed blood vessels in the +MMC group in comparison to the -MMC and control groups. (H) Immunohistochemical staining of human nuclear antigen revealed that the without (−) and with (+) MMC groups retained hADSCs at the site of implantation. All images are at 14 days post-implantation. Scale bar 200 μm. N = 6. (For interpretation of the references to color in this figure legend, the reader is referred to the Web version of this article.)

temperature-responsive film-derived single cell layer scaffold-free systems require a significantly higher cell number and/or days in culture to produce a significantly thinner device (e.g. subject to cell type, 50,000–612,000 cells/cm^2 require 4–28 days in culture to produce devices of 10–50 μm in thickness [72–79]; Supplementary Table S5 provides the details of single layer scaffold-free systems derived from human cells). To increase the thickness of the produced devices, multi-layer cell sheet stacking is used, but this is a multistep process that is notoriously difficult to scale up in reproducible fashion and again requires high cell numbers and prolonged culture times to produce a barely 3D implantable device (e.g. subject to cell type, 3–5 layers of 50,000–1,000,000 cells/cm^2/layer require 5–25 days in culture to produce devices of 20–100 μm in thickness [80–83]; Supplementary Table S6 provides the details of multi-layer scaffold-free systems derived from human cells). It is worth noting that a 350 μm in thickness device has been produced after 7–10 days in culture using 9 layers of 200,000 cells/cm^2/layer

[83]. However, in the absence of sufficient ECM, the very compact conformation of the stacked cell layers results in poor vascularisation, cell death and delamination [19,20,75] and polysurgeries (x10) of up to 3 layers (~80 μm in thickness) are recommended [21] to ultimately result in a neotissue of ~840 μm in thickness. Of course, such work was conducted in an animal model, as patient distress and healthcare expenditure completely negates such approach in humans. With respect to PNIPAM-based temperature-responsive electrospun-derived scaffold-free systems, again our work is of significant importance, as previous studies have only achieved enzyme-free cell separation and failed to produce intact cell sheets [84,85]. Only one study has reported intact cell (human mesenchymal stem cells) sheet detachment from a temperature-responsive electrospun hydroxybutyl-chitosan-collagen (the use of collagen avoided shrinkage and increased cell attachment) scaffold after 14 days in culture [25]; however, cell density/cm^2 and cell sheet thickness were not reported and in the absence of a follow up study, we cannot correlate our data to this work. It is also worth noting, that in our case, cells and *de novo* synthesised and deposited ECM were distributed throughout the thickness of the tissue surrogate. This is again of significant importance, considering that conventional electrospinning setups (like the one used herein) result in very compact electrospun scaffolds with limited cell and tissue infiltration capacity, which gave rise to sacrificial electrospinning [86,87]. We attribute this 3D *in vitro* neotissue formation to the enhanced ECM deposition, due to MMC, that infiltrated the electrospun scaffold and encouraged cell migration. After all, in developing tissues, ECM provides paths that support and coordinate cell migration [88] via integrin adhesion complexes that generate traction forces and are responsible for cell migration to interstitial parts of tissues [89,90].

With respect to safety and efficacy, using a humanised wound healing model, we demonstrated that the MMC derived scaffold-free devices resulted in accelerated wound closure, collagen-rich neotissue formation and reduced scar area, as judged by histochemical and immunohistochemical analysis. We attribute this significantly improved wound closure to the enhanced, due to MMC, ECM deposition that protected and localised cells and their rich in tropic and reparative factors secretome at the side of implantation. This can be further verified by our *in vitro* growth factor and MMPs data that demonstrated that MMC created a balance between enhanced growth factor release from the ECM-rich cellular constructs and increased MMP activity (Supplementary Figure S16 graphically illustrates this activity), which is in agreement with previous publications showing that the release and activation of matrix-embedded growth factors depends on MMP-mediated proteolysis, which ultimately leads to neo-angiogenesis and tissue regeneration [91–94]. It is also worth noting that this is the only scaffold-free device that has resulted in such positive therapeutic efficiency with such low number of cells and short culture period. For example, other studies that utilised the same humanised model and hADSCs, showed slower wound closure using 3 layers of 104,000 cells/cm^2/layer (for unspecified period of time in culture) [95] or 3 layers of 300,000 cells/cm^2/layer cultured for 5 days [81]. Similarly, using the same model, 3 layers of 50,000 human bone marrow stem cells/cm^2/layer cultured for 7 days (20 μm in thickness) also resulted in slower wound closure [96].

5. Conclusions

In vitro organogenesis approaches have failed to produce clinically and commercially relevant implantable devices, largely attributed to the prolonged *ex vivo* culture periods required to develop a barely three-dimensional tissue-like construct that are associated with cell phenotypic drift, loss of cellular function and high manufacturing costs. Herein, macromolecular crowding coupled with a temperature-responsive electrospun scaffold allowed the accelerated development of functional and truly three-dimensional tissue-like surrogates. The proposed approach has the potential to transform cell-assembled regenerative medicine.

Author credit statement

Andrea De Pieri and **Dimitrios I. Zeugolis** designed the study and wrote the manuscript. **Andrea De Pieri**, **Stefanie H. Korntner**, **Hector Capella-Monsonis** and **Dimitrios Tsiapalis** carried out experiments. **Andrea De Pieri** analysed data. **Sergei V. Kostjuk**, **Semyon Churbanov**, **Peter Timashev** and **Yury Rochev** were involved in the synthesis and characterisation (contact angle) of the temperature-responsive polymers. All authors have read, discussed and approved the manuscript.

Declaration of competing interest

The authors declare that they have no known competing financial interests or personal relationships that could have appeared to influence the work reported in this paper.

Data availability

Data will be made available on request.

Acknowledgements

This work has also received funding from the European Union's Horizon 2020 research and innovation programme under the Marie Skłodowska-Curie, grant agreement No. 676338and the European Research Council (ERC) under the European Union's Horizon 2020 research and innovation programme, grant agreement No. 866126. This publication has emanated from research supported by grants from Science Foundation Ireland (SFI) under grant numbers 15/CDA/3629 and 19/FFP/6982and Science Foundation Ireland (SFI) and European Regional Development Fund (ERDF) under grant number 13/RC/2073_2. This work was also supported by the Russian Science Foundation, grant agreement No. 21-15-00349. The authors would like to thank staff at the Geofluid Research Laboratory, Earth and Ocean Sciences, NUI Galway for assistance with the time lapse microscopy. This paper is dedicated to the memory of Prof Alexander Gorelov, who suddenly passed away.

Appendix A. Supplementary data

Supplementary data to this article can be found online at https://doi.org/10.1016/j.biomaterials.2022.121674.

References

[1] J. Schlabe, C. Johnen, R. Schwartlander, V. Moser, B. Hartmann, J.C. Gerlach, M. V. Küntscher, Isolation and culture of different epidermal and dermal cell types from human scalp suitable for the development of a therapeutical cell spray, Burns 34 (3) (2008) 376–384.
[2] H. Ravari, D. Hamidi-Almadari, M. Salimifar, S. Bonakdaran, M.R. Parizadeh, G. Koliakos, Treatment of non-healing wounds with autologous bone marrow cells, platelets, fibrin glue and collagen matrix, Cytotherapy 13 (6) (2011) 705–711.
[3] G. Marino, M. Moraci, E. Armenia, C. Orabona, R. Sergio, G. De Sena, V. Capuozzo, M. Barbarisi, F. Rosso, G. Giordano, F. Iovino, A. Barbarisi, Therapy with autologous adipose-derived regenerative cells for the care of chronic ulcer of lower limbs in patients with peripheral arterial disease, J. Surg. Res. 185 (1) (2013) 36–44.
[4] J. Still, P. Glat, P. Silverstein, J. Griswold, D. Mozingo, The use of a collagen sponge/living cell composite material to treat donor sites in burn patients, Burns 29 (8) (2003) 837–841.
[5] D. Jiang, Y. Qi, N.G. Walker, A. Sindrilaru, A. Hainzl, M. Wlaschek, S. MacNeil, K. Scharffetter-Kochanek, The effect of adipose tissue derived MSCs delivered by a chemically defined carrier on full-thickness cutaneous wound healing, Biomaterials 34 (10) (2013) 2501–2515.
[6] A. Kurtz, Mesenchymal stem cell delivery routes and fate, Int J Stem Cells 1 (1) (2008) 1–7.

[7] T.J. Kean, P. Lin, A.I. Caplan, J.E. Dennis, MSCs: delivery routes and engraftment, cell-targeting strategies, and immune modulation, Stem Cell. Int. 2013 (2013) 732742, 732742.
[8] Y. Ikada, Challenges in tissue engineering, J. R. Soc. Interface 3 (10) (2006) 589–601.
[9] M. Peck, N. Dusserre, T.N. McAllister, N. L'Heureux, Tissue engineering by self-assembly, Mater. Today 14 (5) (2011) 218–224.
[10] D. Thomas, D. Gaspar, A. Sorushanova, G. Milcovich, K. Spanoudes, A.M. Mullen, T. O'Brien, A. Pandit, D.I. Zeugolis, Scaffold and scaffold-free self-assembled systems in regenerative medicine, Biotechnol. Bioeng. 113 (6) (2016) 1155–1163.
[11] H. Takahashi, T. Okano, Thermally-triggered fabrication of cell sheets for tissue engineering and regenerative medicine, Adv. Drug Deliv. Rev. 138 (2019) 276–292.
[12] M. Yamato, T. Okano, Cell sheet engineering, Mater. Today 7 (5) (2004) 42–47.
[13] M.E. Nash, D. Healy, W.M. Carroll, C. Elvira, Y.A. Rochev, Cell and cell sheet recovery from pNIPAm coatings; Motivation and history to present day approaches, J. Mater. Chem. 22 (37) (2012) 19376–19389.
[14] N.A. Dzhoyashvili, K. Thompson, A.V. Gorelov, Y.A. Rochev, Film thickness determines cell growth and cell sheet detachment from spin-coated poly(N-isopropylacrylamide) substrates, ACS Appl. Mater. Interfaces 8 (41) (2016) 27564–27572.
[15] D. Healy, M.E. Nash, A. Gorelov, K. Thompson, P. Dockery, S. Beloshapkin, Y. Rochev, Fabrication and application of photocrosslinked, nanometer-scale, physically adsorbed films for tissue culture regeneration, Macromol. Biosci. 17 (2) (2017).
[16] Y. Haraguchi, T. Shimizu, T. Sasagawa, H. Sekine, K. Sakaguchi, T. Kikuchi, W. Sekine, S. Sekiya, M. Yamato, M. Umezu, T. Okano, Fabrication of functional three-dimensional tissues by stacking cell sheets in vitro, Nat. Protoc. 7 (5) (2012) 850–858.
[17] Y. Tsuda, T. Shimizu, M. Yamato, A. Kikuchi, T. Sasagawa, S. Sekiya, J. Kobayashi, G. Chen, T. Okano, Cellular control of tissue architectures using a three-dimensional tissue fabrication technique, Biomaterials 28 (33) (2007) 4939–4946.
[18] A. De Pieri, Y. Rochev, D.I. Zeugolis, Scaffold-free cell-based tissue engineering therapies: advances, shortfalls and forecast, NPJ Regen Med 6 (1) (2021) 18.
[19] H. Takahashi, M. Nakayama, T. Shimizu, M. Yamato, T. Okano, Anisotropic cell sheets for constructing three-dimensional tissue with well-organized cell orientation, Biomaterials 32 (34) (2011) 8830–8838.
[20] Y. Haraguchi, Y. Kagawa, K. Sakaguchi, K. Matsuura, T. Shimizu, T. Okano, Thicker three-dimensional tissue from a "symbiotic recycling system" combining mammalian cells and algae, Sci. Rep. 7 (2017) 41594, 41594.
[21] T. Shimizu, H. Sekine, J. Yang, Y. Isoi, M. Yamato, A. Kikuchi, E. Kobayashi, T. Okano, Polysurgery of cell sheet grafts overcomes diffusion limits to produce thick, vascularized myocardial tissues, Faseb. J. 20 (6) (2006) 708–710.
[22] K.P. Fuller, D. Gaspar, L.M. Delgado, A. Pandit, D.I. Zeugolis, Influence of porosity and pore shape on structural, mechanical and biological properties of poly ε-caprolactone electro-spun fibrous scaffolds, Nanomedicine (Lond) 11 (9) (2016) 1031–1040.
[23] K.P. Fuller, A. Pandit, D.I. Zeugolis, The multifaceted potential of electro-spinning in regenerative medicine, Pharm. Nanotechnol. 2 (1) (2014) 23–34.
[24] S. Nagarajan, M. Bechelany, N.S. Kalkura, P. Miele, C.P. Bohatier, S. Balme, Chapter 20 - electrospun nanofibers for drug delivery in regenerative medicine, in: S.S. Mohapatra, S. Ranjan, N. Dasgupta, R.K. Mishra, S. Thomas (Eds.), Applications of Targeted Nano Drugs and Delivery Systems, 2019, pp. 595–625. Elsevier.
[25] J.M. Dang, K.W. Leong, Myogenic induction of aligned mesenchymal stem cell sheets by culture on thermally responsive electrospun nanofibers, Adv. Mater. 19 (19) (2007) 2775–2779.
[26] A.C.B. Allen, E. Barone, C.O.K. Crosby, L.J. Suggs, J. Zoldan, Electrospun poly(N-isopropyl acrylamide)/poly(caprolactone) fibers for the generation of anisotropic cell sheets, Biomater. Sci. 5 (8) (2017) 1661–1669.
[27] D.M. Wiese, C.C. Ruttan, C.A. Wood, B.N. Ford, L.R. Braid, Accumulating transcriptome drift precedes cell aging in human umbilical cord-derived mesenchymal stromal cells serially cultured to replicative senescence, Stem Cells Transl Med 8 (9) (2019) 945–958.
[28] A. Schellenberg, T. Stiehl, P. Horn, S. Joussen, N. Pallua, A.D. Ho, W. Wagner, Population dynamics of mesenchymal stromal cells during culture expansion, Cytotherapy 14 (4) (2012) 401–411.
[29] F. Gattazzo, A. Urciuolo, P. Bonaldo, Extracellular matrix: a dynamic microenvironment for stem cell niche, Biochim. Biophys. Acta 1840 (8) (2014) 2506–2519.
[30] F. Guilak, D.M. Cohen, B.T. Estes, J.M. Gimble, W. Liedtke, C.S. Chen, Control of stem cell fate by physical interactions with the extracellular matrix, Cell Stem Cell 5 (1) (2009) 17–26.
[31] F.M. Watt, W.T.S. Huck, Role of the extracellular matrix in regulating stem cell fate, Nat. Rev. Mol. Cell Biol. 14 (8) (2013) 467–473.
[32] A. Kumar, J.K. Placone, A.J. Engler, Understanding the extracellular forces that determine cell fate and maintenance, Development 144 (23) (2017) 4261–4270.
[33] D. Tsiapalis, S. Kearns, J. Kelly, D. Zeugolis, Growth factor and macromolecular crowding supplementation in human tenocyte culture, Biomaterials and Biosystems 1 (2021), 100009.
[34] D. Cigognini, D. Gaspar, P. Kumar, A. Satyam, S. Alagesan, C. Sanz-Nogués, M. Griffin, T. O'Brien, A. Pandit, D.I. Zeugolis, Macromolecular crowding meets oxygen tension in human mesenchymal stem cell culture - a step closer to physiologically relevant in vitro organogenesis, Sci. Rep. 6 (2016), 30746.
[35] D. Tsiapalis, A. De Pieri, K. Spanoudes, I. Sallent, S. Kearns, J.L. Kelly, M. Raghunath, D.I. Zeugolis, The synergistic effect of low oxygen tension and macromolecular crowding in the development of extracellular matrix-rich tendon equivalents, Biofabrication 12 (2) (2020), 025018.
[36] A. Satyam, P. Kumar, D. Cigognini, A. Pandit, D. Zeugolis, Low, but not too low, oxygen tension and macromolecular crowding accelerate extracellular matrix deposition in human dermal fibroblast culture, Acta Biomater. 44 (2016) 221–231.
[37] P. Kumar, A. Satyam, D. Cigognini, A. Pandit, D. Zeugolis, Low oxygen tension and macromolecular crowding accelerate extracellular matrix deposition in human corneal fibroblast culture, J Tissue Eng Regen Med 12 (1) (2018) 6–18.
[38] D. Gaspar, C.N.M. Ryan, D.I. Zeugolis, Multifactorial bottom-up bioengineering approaches for the development of living tissue substitutes, Faseb. J. 33 (4) (2019) 5741–5754.
[39] G. Rivas, A.P. Minton, Macromolecular crowding in vitro, in vivo, and in between, Trends Biochem. Sci. 41 (11) (2016) 970–981.
[40] D. Gnutt, S. Ebbinghaus, The macromolecular crowding effect–from in vitro into the cell, Biol. Chem. 397 (1) (2016) 37–44.
[41] I.M. Kuznetsova, K.K. Turoverov, V.N. Uversky, What macromolecular crowding can do to a protein, Int. J. Mol. Sci. 15 (12) (2014) 23090–23140.
[42] D. Gnutt, M. Gao, O. Brylski, M. Heyden, S. Ebbinghaus, Excluded-volume effects in living cells, Angew Chem. Int. Ed. Engl. 54 (8) (2015) 2548–2551.
[43] M. Tabaka, T. Kalwarczyk, J. Szymanski, S. Hou, R. Holyst, The effect of macromolecular crowding on mobility of biomolecules, association kinetics, and gene expression in living cells, Front. Physiol. 2 (54) (2014).
[44] M. Raghunath, D.I. Zeugolis, Transforming eukaryotic cell culture with macromolecular crowding, Trends Biochem. Sci. 46 (10) (2021) 805–811.
[45] D. Tsiapalis, D.I. Zeugolis, It is time to crowd your cell culture media - physicochemical considerations with biological consequences, Biomaterials 275 (2021), 120943.
[46] D. Gaspar, K.P. Fuller, D.I. Zeugolis, Polydispersity and negative charge are key modulators of extracellular matrix deposition under macromolecular crowding conditions, Acta Biomater. 88 (2019) 197–210.
[47] P. Kumar, A. Satyam, X. Fan, E. Collin, Y. Rochev, B.J. Rodriguez, A. Gorelov, S. Dillon, L. Joshi, M. Raghunath, A. Pandit, D.I. Zeugolis, Macromolecularly crowded in vitro microenvironments accelerate the production of extracellular matrix-rich supramolecular assemblies, Sci. Rep. 5 (2015) 8729.
[48] A. Satyam, P. Kumar, X. Fan, A. Gorelov, Y. Rochev, L. Joshi, H. Peinado, D. Lyden, B. Thomas, B. Rodriguez, M. Raghunath, A. Pandit, D. Zeugolis, Macromolecular crowding meets tissue engineering by self-assembly: a paradigm shift in regenerative medicine, Adv. Mater. 26 (19) (2014) 3024–3034.
[49] R.R. Lareu, K.H. Subramhanya, Y. Peng, P. Benny, C. Chen, Z. Wang, R. Rajagopalan, M. Raghunath, Collagen matrix deposition is dramatically enhanced in vitro when crowded with charged macromolecules: the biological relevance of the excluded volume effect, FEBS Lett. 581 (14) (2007) 2709–2714.
[50] D. Shendi, J. Marzi, W. Linthicum, A.J. Rickards, D.M. Dolivo, S. Keller, M. A. Kauss, Q. Wen, T.C. McDevitt, T. Dominko, K. Schenke-Layland, M.W. Rolle, Hyaluronic acid as a macromolecular crowding agent for production of cell-derived matrices, Acta Biomater. 100 (2019) 292–305.
[51] V. Graceffa, D.I. Zeugolis, Carrageenan enhances chondrogenesis and osteogenesis in human bone marrow stem cell culture, Eur. Cell. Mater. 37 (2019) 310–332.
[52] M. Patrikoski, M.H.C. Lee, L. Mäkinen, X.M. Ang, B. Mannerström, M. Raghunath, S. Miettinen, Effects of macromolecular crowding on human adipose stem cell culture in fetal bovine serum, human serum, and defined xeno-free/serum-free conditions, Stem Cell. Int. 2017 (2017), 6909163.
[53] M.H. Lee, A.G. Goralczyk, R. Kriszt, X.M. Ang, C. Badowski, Y. Li, S.A. Summers, S. A. Toh, M.S. Yassin, A. Shabbir, A. Sheppard, M. Raghunath, ECM microenvironment unlocks brown adipogenic potential of adult human bone marrow-derived MSCs, Sci. Rep. 6 (2016), 21173.
[54] L. Ma, C. Gan, Y. Huang, Y. Wang, G. Luo, J. Wu, Comparative proteomic analysis of extracellular matrix proteins secreted by hypertrophic scar with normal skin fibroblasts, Burns Trauma 2 (2) (2014) 76–83.
[55] A.S. Zeiger, F.C. Loe, R. Li, M. Raghunath, K.J. Van Vliet, Macromolecular crowding directs extracellular matrix organization and mesenchymal stem cell behavior, PLoS One 7 (5) (2012), e37904.
[56] A. De Pieri, S. Rana, S. Korntner, D.I. Zeugolis, Seaweed polysaccharides as macromolecular crowding agents, Int. J. Biol. Macromol. 164 (2020) 434–446.
[57] M.C. Prewitz, A. Stißel, J. Friedrichs, N. Träber, S. Vogler, M. Bornhäuser, C. Werner, Extracellular matrix deposition of bone marrow stroma enhanced by macromolecular crowding, Biomaterials 73 (2015) 60–69.
[58] A. English, A. Azeem, D.A. Gaspar, K. Keane, P. Kumar, M. Keeney, N. Rooney, A. Pandit, D.I. Zeugolis, Preferential cell response to anisotropic electro-spun fibrous scaffolds under tension-free conditions, J. Mater. Sci. Mater. Med. 23 (1) (2012) 137–148.
[59] D.I. Zeugolis, S.T. Khew, E.S.Y. Yew, A.K. Ekaputra, Y.W. Tong, L.-Y.L. Yung, D. W. Hutmacher, C. Sheppard, M. Raghunath, Electro-spinning of pure collagen nano-fibres – just an expensive way to make gelatin? Biomaterials 29 (15) (2008) 2293–2305.
[60] H. Capella-Monsonís, J.Q. Coentro, V. Graceffa, Z. Wu, D.I. Zeugolis, An experimental toolbox for characterization of mammalian collagen type I in biological specimens, Nat. Protoc. 13 (2018) 507.
[61] H.K. Graham, N.W. Hodson, J.A. Hoyland, S.J. Millward-Sadler, D. Garrod, A. Scothern, C.E.M. Griffiths, R.E.B. Watson, T.R. Cox, J.T. Erler, A.W. Trafford, M. J. Sherratt, Tissue section AFM: in situ ultrastructural imaging of native biomolecules, Matrix Biol. 29 (4) (2010) 254–260.
[62] C.C. Liang, A.Y. Park, J.L. Guan, In vitro scratch assay: a convenient and inexpensive method for analysis of cell migration in vitro, Nat. Protoc. 2 (2) (2007) 329–333.

[63] S. Kroening, M. Goppelt-Struebe, Analysis of matrix-dependent cell migration with a barrier migration assay, Sci. Signal. 3 (126) (2010) pl1.
[64] X. Wang, J. Ge, E.E. Tredget, Y. Wu, The mouse excisional wound splinting model, including applications for stem cell transplantation, Nat. Protoc. 8 (2) (2013) 302–309.
[65] H. Khorasani, Z. Zheng, C. Nguyen, J. Zara, X. Zhang, J. Wang, K. Ting, C. Soo, A quantitative approach to scar analysis, Am. J. Pathol. 178 (2) (2011) 621–628.
[66] Selezneva II, A.V. Gorelov, Y.A. Rochev, Use of thermosensitive polymer material on the basis of N-isopropylacrylamide and N-tert-butylacrylamide copolymer in cell technologies, Bull. Exp. Biol. Med. 142 (4) (2006) 538–541.
[67] Y. Rochev, D. O'Halloran, T. Gorelova, V. Gilcreest, I. Selezneva, B. Gavrilyuk, A. Gorelov, Rationalising the design of polymeric thermoresponsive biomaterials, J. Mater. Sci. Mater. Med. 15 (4) (2004) 513–517.
[68] O.H. Kwon, A. Kikuchi, M. Yamato, Y. Sakurai, T. Okano, Rapid cell sheet detachment from poly(N-isopropylacrylamide)-grafted porous cell culture membranes, J. Biomed. Mater. Res. 50 (1) (2000) 82–89.
[69] O. Hyeong Kwon, A. Kikuchi, M. Yamato, T. Okano, Accelerated cell sheet recovery by co-grafting of PEG with PIPAAm onto porous cell culture membranes, Biomaterials 24 (7) (2003) 1223–1232.
[70] H. Takahashi, T. Okano, Cell sheet-based tissue engineering for organizing anisotropic tissue constructs produced using microfabricated thermoresponsive substrates, Adv Healthc Mater 4 (16) (2015) 2388–2407.
[71] T. Sasagawa, T. Shimizu, S. Sekiya, Y. Haraguchi, M. Yamato, Y. Sawa, T. Okano, Design of prevascularized three-dimensional cell-dense tissues using a cell sheet stacking manipulation technology, Biomaterials 31 (7) (2010) 1646–1654.
[72] K. Yamamoto, M. Yamato, T. Morino, H. Sugiyama, R. Takagi, Y. Yaguchi, T. Okano, H. Kojima, Middle ear mucosal regeneration by tissue-engineered cell sheet transplantation, NPJ Regen Med 2 (2017) 6.
[73] H. Masumoto, T. Ikuno, M. Takeda, H. Fukushima, A. Marui, S. Katayama, T. Shimizu, T. Ikeda, T. Okano, R. Sakata, J.K. Yamashita, Human iPS cell-engineered cardiac tissue sheets with cardiomyocytes and vascular cells for cardiac regeneration, Sci. Rep. 4 (2014) 6716.
[74] R. Takagi, D. Murakami, M. Kondo, T. Ohki, R. Sasaki, M. Mizutani, M. Yamato, K. Nishida, H. Namiki, M. Yamamoto, T. Okano, Fabrication of human oral mucosal epithelial cell sheets for treatment of esophageal ulceration by endoscopic submucosal dissection, Gastrointest. Endosc. 72 (6) (2010) 1253–1259.
[75] W. Sekine, Y. Haraguchi, T. Shimizu, A. Umezawa, T. Okano, Thickness limitation and cell viability of multi-layered cell sheets and overcoming the diffusion limit by a porous-membrane culture insert, J. Biochips Tissue Chips S2 (2011).
[76] H. Okura, A. Matsuyama, C.M. Lee, A. Saga, A. Kakuta-Yamamoto, A. Nagao, N. Sougawa, N. Sekiya, K. Takekita, Y. Shudo, S. Miyagawa, H. Komoda, T. Okano, Y. Sawa, Cardiomyoblast-like cells differentiated from human adipose tissue-derived mesenchymal stem cells improve left ventricular dysfunction and survival in a rat myocardial infarction model, Tissue Eng. C Methods 16 (3) (2010) 417–425.
[77] W. Sekine, Y. Haraguchi, T. Shimizu, M. Yamato, A. Umezawa, T. Okano, Chondrocyte differentiation of human endometrial gland-derived MSCs in layered cell sheets, Sci. World J. 2013 (2013), 359109.
[78] M. Ishigami, H. Masumoto, T. Ikuno, T. Aoki, M. Kawatou, K. Minakata, T. Ikeda, R. Sakata, J.K. Yamashita, K. Minatoya, Human iPS cell-derived cardiac tissue sheets for functional restoration of infarcted porcine hearts, PLoS One 13 (8) (2018), e0201650.
[79] T. Sumide, K. Nishida, M. Yamato, T. Ide, Y. Hayashida, K. Watanabe, J. Yang, C. Kohno, A. Kikuchi, N. Maeda, H. Watanabe, T. Okano, Y. Tano, Functional human corneal endothelial cell sheets harvested from temperature-responsive culture surfaces, Faseb. J. 20 (2) (2006) 392–394.
[80] M. Sato, M. Yamato, G. Mitani, T. Takagaki, K. Hamahashi, Y. Nakamura, M. Ishihara, R. Matoba, H. Kobayashi, T. Okano, J. Mochida, M. Watanabe, Combined surgery and chondrocyte cell-sheet transplantation improves clinical and structural outcomes in knee osteoarthritis, NPJ Regen Med 4 (2019) 4.
[81] M.T. Cerqueira, R.P. Pirraco, T.C. Santos, D.B. Rodrigues, A.M. Frias, A.R. Martins, R.L. Reis, A.P. Marques, Human adipose stem cells cell sheet constructs impact epidermal morphogenesis in full-thickness excisional wounds, Biomacromolecules 14 (11) (2013) 3997–4008.
[82] T. Kikuchi, T. Shimizu, M. Wada, M. Yamato, T. Okano, Automatic fabrication of 3-dimensional tissues using cell sheet manipulator technique, Biomaterials 35 (8) (2014) 2428–2435.
[83] H. Komae, H. Sekine, I. Dobashi, K. Matsuura, M. Ono, T. Okano, T. Shimizu, Three-dimensional functional human myocardial tissues fabricated from induced pluripotent stem cells, J Tissue Eng Regen Med 11 (3) (2017) 926–935.
[84] K. Nagase, R. Shukuwa, H. Takahashi, N. Takeda, T. Okano, Enhanced mechanical properties and cell separation with thermal control of PIPAAm-brushed polymer-blend microfibers, J. Mater. Chem. B 8 (28) (2020) 6017–6026.
[85] K. Nagase, Y. Sakurada, S. Onizuka, T. Iwata, M. Yamato, N. Takeda, T. Okano, Thermoresponsive polymer-modified microfibers for cell separations, Acta Biomater. 53 (2017) 81–92.
[86] N. Kasoju, J. George, H. Ye, Z. Cui, Sacrificial core-based electrospinning: a facile and versatile approach to fabricate devices for potential cell and tissue encapsulation applications, Nanomaterials 8 (10) (2018).
[87] J. Voorneveld, A. Oosthuysen, T. Franz, P. Zilla, D. Bezuidenhout, Dual electrospinning with sacrificial fibers for engineered porosity and enhancement of tissue ingrowth, J. Biomed. Mater. Res. B Appl. Biomater. 105 (6) (2017) 1559–1572.
[88] D.A.C. Walma, K.M. Yamada, The extracellular matrix in development, Development 147 (10) (2020) dev175596.
[89] T. Rozario, D.W. DeSimone, The extracellular matrix in development and morphogenesis: a dynamic view, Dev. Biol. 341 (1) (2010) 126–140.
[90] S. van Helvert, C. Storm, P. Friedl, Mechanoreciprocity in cell migration, Nat. Cell Biol. 20 (1) (2018) 8–20.
[91] D. Rodríguez, C.J. Morrison, C.M. Overall, Matrix metalloproteinases: what do they not do? New substrates and biological roles identified by murine models and proteomics, Biochim. Biophys. Acta 1803 (1) (2010) 39–54.
[92] J.D. Mott, Z. Werb, Regulation of matrix biology by matrix metalloproteinases, Curr. Opin. Cell Biol. 16 (5) (2004) 558–564.
[93] R.A. Dean, G.S. Butler, Y. Hamma-Kourbali, J. Delbé, D.R. Brigstock, J. Courty, C. M. Overall, Identification of candidate angiogenic inhibitors processed by matrix metalloproteinase 2 (MMP-2) in cell-based proteomic screens: disruption of vascular endothelial growth factor (VEGF)/Heparin affin regulatory peptide (Pleiotrophin) and VEGF/connective tissue growth factor angiogenic inhibitory iomplexes by MMP-2 proteolysis, Mol. Cell Biol. 27 (24) (2007) 8454–8465.
[94] Q. Yu, I. Stamenkovic, Cell surface-localized matrix metalloproteinase-9 proteolytically activates TGF-beta and promotes tumor invasion and angiogenesis, Genes Dev. 14 (2) (2000) 163–176.
[95] Y.C. Lin, T. Grahovac, S.J. Oh, M. Ieraci, J.P. Rubin, K.G. Marra, Evaluation of a multi-layer adipose-derived stem cell sheet in a full-thickness wound healing model, Acta Biomater. 9 (2) (2013) 5243–5250.
[96] M.-A. Koo, S. Hee Hong, M. Hee Lee, B.-J. Kwon, G. Mi Seon, M. Sung Kim, D. Kim, K. Chang Nam, J.-C. Park, Effective stacking and transplantation of stem cell sheets using exogenous ROS-producing film for accelerated wound healing, Acta Biomater. 95 (2019) 418–426.